Semiflexible Polymers and Filaments: From Variational Problems to Fluctuations

Jan Kierfeld*,†, Krzysztof Baczynski†, Petra Gutjahr† and Reinhard Lipowsky†

*Physics Department, Dortmund University of Technology, 44221 Dortmund, Germany
†Max Planck Institute of Colloids and Interfaces, Science Park Golm, 14424 Potsdam, Germany

Abstract. We discuss shapes and shape fluctuations of semiflexible polymers or filaments, which are polymers with an appreciable bending rigidity. The physical properties of semiflexible polymers are governed by their persistence length. On length scales smaller than the persistence length thermal fluctuations can be neglected and polymer shapes are obtained by bending energy minimization. On length scales larger than the persistence length, however, thermal shape fluctuations play an important role and cannot be neglected in general. After a general definition of the persistence length based on the bending rigidity renormalization we will review some problems related to single semiflexible polymers where both variational problems of energy minimization and thermal fluctuations play an important role. We will discuss the buckling instability of semiflexible polymers, their force-induced desorption, and the shapes of adsorbed semiflexible polymers on structured substrates.

Keywords: Semiflexible Polymers, Filaments, Persistence length, Buckling, Ring polymers, Adsorption, Desorption
PACS: 02.30.Xx, 05.10.Cc, 46.32.+x, 82.35.Gh, 87.16.Dg, 87.16.Ka

INTRODUCTION

Many polymers in chemical and biological physics behave as flexible chains with segments that can freely rotate against each other. Such flexible polymers are governed by an entropic tension, which tends to minimize the end-to-end distance in order to maximize the number of possible chain conformations. Typical examples of flexible polymers are synthetic polymers with a carbon backbone, such as polyethylene, where the carbon-carbon bonds along the backbone can easily rotate against each other. By now, there is a rather complete theoretical description of flexible polymers [1, 2, 3], which includes both statics and dynamics, effects from self-avoidance, and the cooperative behavior of flexible polymers in solutions or gels.

Apart from flexible polymers, there is another important class of more rigid polymers, which are governed by their bending energy rather than their entropic tension over a wide range of length scales. The competition between thermal energy and the bending energy of the polymer sets a characteristic length scale, the *persistence length*,

$$L_p \equiv \frac{2}{d-1}\frac{\kappa}{T} \tag{1}$$

where κ is the bending rigidity of the polymer and T the temperature (in the following we will use energy units, i.e., the Boltzmann constant k_B is contained in the symbol T) and d the number of spatial dimensions of the embedding space. Physically relevant

CP1002, *Curvature and Variational Modeling in Physics and Biophysics*
edited by O. J. Garay, E. García-Río, and R. Vázquez-Lorenzo

cases are polymers in three spatial dimensions ($d = 3$) and polymers, which are adsorbed on a planar substrate and, thus, confined to two dimensions ($d = 2$). We will give a detailed derivation of the persistence length (1) below. In short, the persistence length can be characterized as the length scale above which tangent-tangent correlations decay exponentially, see eq. (3) below.

On length scales much larger than L_p, any polymer behaves as a flexible chain with a segment size of the order of L_p, i.e., the polymer decays into effectively independent segments of size L_p. For large values of the persistence length, the polymer attains the limit of a rigid rod, deformations of which are described by classical mechanics [4], i.e., by minimization of the bending energy of the polymer. We will be interested in *semiflexible polymers*, which can be defined as polymers with a persistence length that is not infinite, but large enough that it becomes comparable to other important length scales governing the polymer's behavior. For a single free polymer, for example, the only other length scale which is relevant is its contour length, and we call the polymer semiflexible if the persistence length becomes of the order of the contour length. In this review, we will focus both on the regime where the persistence length is very large and the effects of thermal fluctuations can be neglected, such that we are dealing with the variational problem of minimizing the bending energy and on the semiflexible regime, where thermal fluctuations start to become relevant.

In biological and chemical physics one finds many examples of semiflexible polymers or "nanorods". Typically, these polymers are supramolecular assemblies with a relatively large diameter, which can vary between about one nanometer and tens of nanometers, i.e., they have a high molecular weight per monomer and are much "thicker" than a flexible synthetic polymer with a carbon backbone. Such polymers are generically semiflexible because their large diameter leads to stronger entropic or enthalpic interactions along their backbones, which increases the bending rigidity. Often these thick supramolecular structures are the result of a rather complicated assembly process. Recent examples from chemical physics are provided by dendronized polymers [5], polyisocyanides (in particular, polyisocanidepeptides [6]), and many supramolecular polymers, such as polyelectrolyte complexes [7]. Another prominent example are carbon nanotubes, which can be viewed as a two-dimensional graphene sheet rolled into a quasi-one-dimensional tubular structure hold together by many carbon bonds. Single-walled carbon nanotubes have a diameter $D \simeq 1 - 2\text{nm}$ and a persistence length $L_p \simeq 1.5\mu\text{m}$ [8] (for $d = 3$). In biological physics an important example for a semiflexible polymer is double-stranded DNA, the carrier of the genetic code, with a mechanical persistence length of 50nm [9] (for $d = 3$). Other important examples are cytoskeletal filaments, such as filamentous (F-) actin and microtubules, or other protein fibers such as sickle hemoglobin (HbS) fibers. Cytoskeletal filaments, such as filamentous (F-) actin and microtubules, are supramolecular structures, which assemble spontaneously from globular protein monomers [10, 11, 12]. F-actin assembles from globular (G-) actin monomers, microtubules from tubulin monomers. These monomers bind by weak non-covalent bonds, typically each monomer binds by several hydrogen bonds. Therefore, cytoskeletal filaments represent self-assembled rod-like structures, sometimes called association

colloids, rather than macromolecules that are connected by covalent bonds. [1] The persistence lengths of cytoskeletal filaments range from 15μm for F-actin [13, 14, 15] (with a diameter of $D \simeq 7$nm and in $d = 3$) to the mm-range for microtubules [14] (which have a diameter of $D \simeq 25$nm) and is comparable to typical contour lengths of these polymers.

It is instructive to estimate the bending rigidity of large supramolecular filaments by modeling them in a simplified manner as an isotropic elastic rod made from an isotropic elastic material with Young's modulus E. For such rods, elasticity theory [4] gives a bending rigidity $\kappa = EI$, where I is the moment of inertia of the rod's cross section S_{cross}, $I \equiv \int_{S_{\text{cross}}} r^2 dS$, which is given by the surface integral over the square of the radius r. Therefore, $I \propto D^4$, where D is the filament diameter, and the persistence length $L_p \sim EI/T \propto D^4$ strongly increases with the filament diameter, i.e., thick filaments are much more rigid. For a filament diameter from 5 to 25nm and an elastic modulus $E \sim 1$GPa, persistence lengths $L_p \sim EI/T$ from 10 to 600 μm are estimated. This simple model thus explains why thick filaments, such as microtubules with a diameter of 25 nm, are much stiffer than slender filaments like F-actin with a diameter of 8nm. The elastic description works well for cytoskeletal filaments because they assemble from relatively large protein monomers; globular (G-) actin, for example, has a molecular weight of 43kD.

Large supramolecular assemblies often form helices to optimize enthalpic interactions, which then also increases the rigidity. Filamentous actin, for example, assembles into a two-stranded helical structure. Another prominent example of a semiflexible helical polymer is DNA. The DNA helix forms as a result of the stacking interactions between planar nucleotide base pairs, which in turn arise from the hydrophobicity of the base pairs and electronic interactions. The helical structure allows base pairs to move closer and expel water from the space between bases. Both in F-actin and DNA the helical structure increases attractive interactions between monomers and increases the bending rigidity. The bending rigidity of a polymer is also increased by repulsive electrostatic interactions between unscreened charges along the polymer backbone [16]. The additional electrostatic contribution to the persistence length leads to a stiffening of charged polymers at low salt concentrations. At physiological salt concentrations, the Debye-Hückel screening length is $l_{DH} \simeq 1$nm so that we can usually neglect electrostatic interactions in modeling cytoskeletal filaments.

Typically, we are interested in fluctuations of semiflexible polymers on the scale of the persistence length such that molecular details are not relevant and a continuous description is justified. Moreover, many semiflexible polymers of interest, like F-actin, microtubules, or DNA, are inextensible to a good approximation. Then they can be modeled by the so-called *worm-like chain (WLC) model* introduced by Kratky and Porod [17] to interpret X-ray scattering experiments on solutions of "filamentous" polymers, e.g., cellulose. Their WLC model describes an inextensible continuous polymer governed by

[1] It is interesting to note that, at the beginning of the 20th century, all polymers were viewed as association colloids, whereas, nowadays, most scientists follow the terminology of Hermann Staudinger and use the term "polymer" as a synonym for a chain-like macromolecule.

its bending energy

$$\mathscr{H}_{\mathrm{WLC}}[\mathbf{t}(s)] = \int_0^L ds \frac{\kappa}{2} (\partial_s \mathbf{t})^2 \quad \text{with } \mathbf{t}^2(s) = 1. \tag{2}$$

Here, L is the contour length of the polymer, which is parameterized by its arc length s, and the polymer configuration is described by the unit tangent vectors $\mathbf{t}(s)$ so that $(\partial_s \mathbf{t})^2$ is the square of the local curvature. In the corresponding partition sum of the worm-like chain model we have to sum over all configurations of unit tangent vectors. The unit length constraint makes the statistical physics of the worm-like chain model non-trivial and equivalent to the one-dimensional non-linear σ-model. Tangent correlations decay exponentially, and in d spatial dimensions one finds [17, 18, 19]

$$\langle \mathbf{t}(s) \cdot \mathbf{t}(s') \rangle = \exp\left(-\frac{|s - s'|}{L_p} \right). \tag{3}$$

For $L \gg L_p$, the worm-like chain can then be described as an effective Gaussian chain with $N = L/L_p$ segments with Kuhn length $b \sim L_p$. Internal interaction potentials, such as, e.g., the excluded volume interaction between different parts of the chain, are neglected in the worm-like chain model. This approximation can be justified as long as the bending rigidity is sufficiently large such that the persistence length L_p is of the same order as the contour length L of the polymer. Then the bending energy is effectively preventing intra-polymer contacts.

During the past decade single-molecule techniques, such as atomic force microscopy (AFM) [20], optical [21] and magnetic tweezers [22], have become available which allow to measure mechanical properties of *individual* molecules and polymers. These techniques give a force resolution in the piconewton range and a spatial resolution in the nanometer regime. Experiments on individual molecules allow to measure distribution functions of observables independent of the spatial averaging, which is always present in usual bulk measurements. Other observables are not directly accessible in a bulk measurement, for example, the extension of a single polymer chain can only be deduced indirectly from scattering experiments in the bulk. Single-molecule techniques are also most suited to study dynamical fluctuations of individual molecules in or out of equilibrium. Applied to polymers, these techniques permit quantitative experimental studies of single polymer deformations and, thus, provide the basis for a quantitative understanding of the mechanical properties of more complex polymer assemblies, such as polymer solutions, gels, or the cytoskeleton of a living cell.

In this review we discuss a number of properties of single semiflexible polymers, which are accessible to such single molecule experiments. The buckling instability of a semiflexible polymer is one example. An elastic rod undergoes a buckling instability if the compressional force F exceeds a certain threshold value. Such buckling instabilities also play a role in biological systems, whenever rigid filaments or semiflexible polymers, such as cytoskeletal filaments or DNA, are under a compressive load. In a single molecule experiment it has been shown that polymerization forces are sufficient to buckle microtubules of micrometer length [23], and the shape of buckled microtubules growing against a hard obstacle has been analyzed to measure microtubule polymerization forces, which were found to lie in the piconewton range.

Novel types of single molecule manipulation experiments become possible with *adsorbed* semiflexible polymers because both visualization and manipulation are easier for adsorbed polymers [24, 25]. In this review we will discuss two single polymer manipulation experiments for adsorbed semiflexible polymers, the force-induced desorption and the forced sliding over an adhesive substrate. Force-induced desorption has been realized experimentally by attaching single polymers to AFM tips, which allows to measure the force exerted by the polymer as a function of the distance from the adsorbing substrate [26]. The force-induced desorption is similar to another type of single molecule manipulation experiment, the unzipping of two semiflexible polymers. Unzipping of polymers has first been studied for the unzipping of the two rather flexible strands of DNA [27] but has recently also been realized for much stiffer protein fibers [28]. Single polymers or other molecules on surfaces can be imaged using scanning tunneling microscopy (STM) [29] on metal or semiconductor surfaces or atomic force microscopy (AFM) [20]. These techniques do not only permit imaging on the surface but the microscopy tips can also be used to manipulate and position individual molecules [30] or individual semiflexible polymers such as DNA [31] on the substrate. In addition, the adsorbing substrate can be modified chemically or lithographically to present a patterned surface structure to the adsorbing polymer, which typically leads to contrasts in adsorption strength. The spatial extension of these regular structures ranges from the micrometer scale down to nanometers. The interaction with a structured substrate surface can be exploited for the immobilization and controlled manipulation of semiflexible polymers which is an important requirement for applications in bionanotechnology.

In comparison to flexible polymers, semiflexible polymers exhibit a more diverse and versatile behavior. First, they exhibit a variety of interesting shapes as obtained from the first variation of the bending energy. From the viewpoint of statistical physics, these shapes represent the states of the polymers at zero temperature. Furthermore, at nonzero temperature, these polymers undergo thermally excited shape fluctuations that "renormalize" their properties and can induce transitions between these different shapes. All shapes of minimal bending energy – the shapes of buckled filaments, the shapes of semiflexible polymer rings adhered to a striped substrate, or the shape of a desorbing polymer – are built from segments of Euler Elastica. These non-trivial minimal energy shapes are subject to thermal fluctuations which can modify the results strongly if the persistence length of the semiflexible polymer becomes comparable to other relevant length scales of the problem.

This article is organized as follows. In the following section "Persistence Length" we introduce a generalized definition of the persistence length based on a renormalization group analysis. In the section "Buckling of Semiflexible Polymers", we consider the buckling instability, in particular the effects of thermal fluctuations on the classical mechanical buckling problem. Then we consider problems related to adsorbed semiflexible polymers. In the section "Adsorption and Desorption", we study force-induced desorption both at zero temperature and taking into account the combined effects of force and temperature. In the section "Semiflexible Polymers on Structured Substrates", we investigate morphologies of adsorbed semiflexible polymers, in particular semiflexible rings, on substrates containing stripe surface structures before we end with conclusions and an outlook.

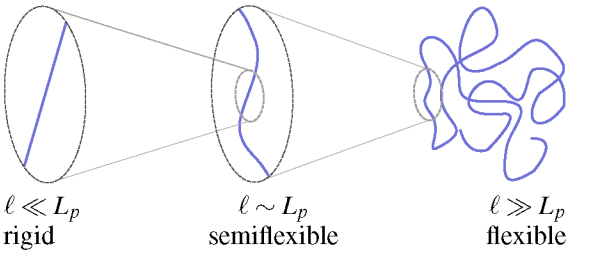

FIGURE 1. Schematic view of a thermally fluctuating semiflexible polymer on different length scales ℓ. On very short length scales $\ell \ll L_p$ the thermal energy is not sufficient to introduce a bend in the contour of the semiflexible polymer (left), whereas on large scales $\ell \gg L_p$ the conformational entropy dominates, so that the orientational order is completely destroyed (right). The intermediate regime $\ell \sim L_p$ is characterized by a subtle competition between thermal fluctuations and the stiffness of the semiflexible polymer (middle).

PERSISTENCE LENGTH

Thermal fluctuations of one-dimensional semiflexible polymers or filaments are governed by their bending energy and can be characterized using the concept of a *persistence length* L_p, which is illustrated in Fig. 1. In the absence of thermal fluctuations at zero temperature, semiflexible polymers are straight because of their bending rigidity. Sufficiently large and thermally fluctuating membranes or semiflexible polymers lose their planar or straight conformation. Only subsystems of size $\ell \ll L_p$ appear rigid and maintain an average planar or straight conformation with a preferred normal or tangent direction, respectively. Membrane patches or polymer segments of sizes $\ell \gg L_p$, on the other hand, appear flexible. In the "semiflexible" regime $\ell \sim L_p$ the statistical mechanics is governed by the competition of the thermal energy T and the bending rigidity κ.

The persistence length L_p of semiflexible polymers is usually defined by the characteristic length scale for the exponential decay of the two-point correlation function between unit tangent vectors $\mathbf{t}$ along the polymer, see eq. (3). The exponential decay of the tangent correlations can also be interpreted as the result of a softening of a semiflexible polymer on large length scales, which is caused by a coupling between bending modes of different wave lengths. This effect can be quantified using renormalization group (RG) methods. Here, we want to present our results for the persistence length from this more general approach, which employs an exact real-space RG scheme for the bending rigidity of a semiflexible polymer to define the persistence length as the characteristic decay length of the renormalized bending rigidity [32].

This problem is not only of interest in the context of one-dimensional semiflexible polymers or filaments. Fluid membranes are objects with two internal dimensions and are also governed by their bending rigidity. For fluid membranes, the quantity which is analogous to the tangent correlations function (3) is the correlation function of normal vectors. An approximate result has been given in Ref. [33], but a rigorous treatment is missing because of the more involved differential geometry. Surfaces cannot be fully determined by specifying an arbitrary set of normal vectors, but have to fulfill additional compatibility conditions in terms of the metric and curvature tensors, the equations of

Gauss, Mainardi and Codazzi, which ensure their continuity. Implementations of these constraints lead to a considerably more complicated field theory than (2) describing a two-dimensional fluid membrane in terms of its normal and tangent vector fields [34].

For two-dimensional fluid membranes, an alternative definition of the persistence length L_p has been given, which is linked to the effect of bending rigidity renormalization. The mode coupling between thermal shape fluctuations of different wave lengths modifies the large scale bending behavior, which can be described by an effective or *renormalized* bending rigidity κ. The renormalized κ has been calculated using different perturbative renormalization group (RG) approaches [35, 36, 37, 38, 39, 40]. The results are still controversial: Several authors [35, 36, 37, 38] find a thermal softening of the membrane with increasing length scales, but differing prefactors, whereas Pinnow and Helfrich [40] obtained the opposite result. Furthermore, different definitions of the persistence length are considered in these approaches: In Refs. [36, 37, 38], L_p is identified with the length scale, where the renormalized bending rigidity κ vanishes, while Helfrich and Pinnow defined L_p via the averaged absorbed area [35, 40]. Whereas the correct bending rigidity renormalization of two-dimensional fluid membranes is still a matter of controversy, we want to present a real-space RG scheme for the bending rigidity renormalization for the one-dimensional case of a semiflexible polymer or a one-dimensional fluid membrane, which allows us to define the persistence length as the characteristic decay length of the renormalized bending rigidity.

In principle, a perturbative result for the effective κ can be deduced from the RG analysis of the one-dimensional nonlinear σ-model, which is equivalent to the WLC Hamiltonian (2). After a Wilson-type momentum-shell RG analysis, one obtains a renormalized reduced effective rigidity $\kappa = \kappa(\ell)$, which depends on the length scale ℓ up to which fluctuations have been integrated in the partition sum. The persistence length can be defined by the condition $\kappa(L_p) \equiv 0$ leading to $L_p \simeq \pi^2 \kappa/(d-2)T$. For the case of the polymer in the plane ($d = 2$), the Hamiltonian simplifies to a free or Gaussian field theory such that κ is unrenormalized to all orders and, thus, the resulting L_p would become infinitely large.

A similar perturbative momentum-shell RG procedure is possible in the so-called Monge parametrization of a weakly bent semiflexible polymer, analogous to the RG analysis for two-dimensional membranes [36]. Then the polymer is parametrized by its projected length x with $0 < x < L_x$, where L_x is the fixed *projected* length of the semiflexible polymer, while its contour length becomes a fluctuating quantity. The renormalized $\kappa = \kappa(\ell_x)$ becomes a function of the projected length scale ℓ_x. Using the analogous criterion $\kappa(L_p) = 0$ we obtain $L_p \simeq 2\pi^2 \kappa/(3d-1)T$ within this approach.

A comparison of the RG results from the non-linear σ-model and the one obtained in the Monge parametrization with eq. (3) for the tangent correlations shows that the RG results for the persistence length L_p are incompatible with each other and with the result (1) based on the tangent correlation function (3). In order to resolve these discrepancies we use a discrete description for semiflexible polymers, which is equivalent to the one-dimensional classical Heisenberg model. This model has the advantage that the κ-renormalization as well as the tangent correlation function are exactly computable in arbitrary dimensions d. Consequently a direct comparison of the persistence length determined via κ-renormalization and via the tangent correlation function is possible.

A discretization of the WLC Hamiltonian (2) should preserve its local inextensibility.

In addition, we want to use a discretized Hamiltonian, which is locally invariant with respect to full rotations of single tangents $\mathbf{t}_i$ – in addition to the global rotational symmetry of the polymer as a whole. A suitable discrete model is an inextensible semiflexible chain model as given by [41]

$$\mathscr{H}\{\mathbf{t}_i\} = \frac{\kappa_0}{b_0}\sum_{i=1}^{M}(1-\mathbf{t}_i\cdot\mathbf{t}_{i-1}), \quad \text{with } \mathbf{t}_i^2 = 1, \tag{4}$$

with M bonds or chain segments of fixed length b_0. In the following we denote the "bare" parameters before renormalization by κ_0 and b_0. The semiflexible chain model is equivalent to the one-dimensional classical Heisenberg model (except for the first term, which represents a constant energy term) describing a one-dimensional chain of classical spins.

The partition sum reads

$$Z_M = \left(\prod_{j=0}^{M}\int d\mathbf{t}_j\right)\exp[-\mathscr{H}\{\mathbf{t}_j\}/T] = \left(\prod_{j=0}^{M}\int d\mathbf{t}_j\right)\prod_{i=1}^{M}T_{i,i-1}\,, \tag{5}$$

where we have introduced the transfer matrix

$$T_{i,i-1} = \exp\left[-K_0(1-\mathbf{t}_i\cdot\mathbf{t}_{i-1})\right], \quad \text{with } K_0 \equiv \kappa_0/b_0T. \tag{6}$$

We can parametrize the scalar product of unit tangent vectors using the azimuthal angle difference $\Delta\theta_{i,i-1}$ as $\mathbf{t}_i\cdot\mathbf{t}_{i-1} = \cos(\Delta\theta_{i,i-1})$. Then the transfer matrix can be expanded as

$$T_{i,i-1} = \sum_{m=-\infty}^{\infty}\lambda_m^{(0)}e^{im\Delta\theta_{i,i-1}}, \;\; \lambda_m^{(0)}(K_0) = e^{-K_0}I_m(K_0) \tag{7}$$

in two dimensions and

$$T_{i,i-1} = \sum_{l=0}^{\infty}(2l+1)\lambda_l^{(0)}P_l(\cos\Delta\theta_{i,i-1}), \;\; \lambda_l^{(0)}(K_0) = \sqrt{\frac{\pi}{2K_0}}e^{-K_0}I_{l+1/2}(K_0) \tag{8}$$

in three dimensions, where $I_k(x)$ denotes the modified Bessel function of the first kind and $P_l(x)$ the Legendre polynomials [42]. In the following, the sums $\sum_{m=-\infty}^{\infty}$ for $d=2$ and $\sum_{l=0}^{\infty}(2l+1)$ for $d=3$ are abbreviated by $\sum_n^{(d)}$.

For simplicity, we restricted our analysis to $d=2$ and $d=3$ spatial dimensions, but our results can easily be generalized to arbitrary dimensions d: The transfer matrix is then expanded in Gegenbauer polynomials and the eigenvalues $\lambda_l^{(0)}$ are proportional to modified Bessel functions $I_{l+d/2-1}(K_0)$.

The real-space functional RG analysis for the semiflexible chain (4) proceeds in close analogy to the one-dimensional Heisenberg model [43] and similarly to the Ising-like case where the $\mathbf{t}_i$'s are confined to discrete values [44]. Similar real-space functional RG methods have also been used to study wetting transitions or the unbinding transitions of strings [45, 46]. In each RG step, every second tangent degree of freedom is eliminated. We introduce a general transfer matrix

$$T_{i,i-1} = \exp\left[h(\mathbf{t}_i\cdot\mathbf{t}_{i-1}, K)\right], \tag{9}$$

where $h = h(u,K)$ defines an *arbitrary* interaction function depending on the scalar product of adjacent tangents $u = \mathbf{t}_i \cdot \mathbf{t}_{i-1}$ and the parameter K. We start the RG procedure with an initial value $K = K_0$ and an initial interaction function $h(u,K) = -K(1-u)$, see eq. (6). Also for an arbitrary interaction function $h(u,K)$ we can expand the transfer matrix in the same sets of functions as in (7) and (8), which defines eigenvalues $\lambda_m = \lambda_m(K)$ in two dimensions and $\lambda_l = \lambda_l(K)$ in three dimensions. Initially, these eigenvalues are given by $\lambda_m(K) = \lambda_m^{(0)}(K)$ and $\lambda_m(K) = \lambda_l^{(0)}(K)$, see (7), (8).

Integration over one intermediate tangent $\mathbf{t}'$ between $\mathbf{t}$ and $\mathbf{t}''$ defines a recursion formula resulting in a new interaction function $h' = h'(u,K)$ and an energy shift g' by

$$\exp[h'(\mathbf{t}\cdot\mathbf{t}'',K) + g'(K)] = \int d\mathbf{t}' \exp[h(\mathbf{t}\cdot\mathbf{t}',K) + h(\mathbf{t}'\cdot\mathbf{t}'',K)], \tag{10}$$

where the energy shift g' is determined by the condition that $h'(1,K) = h(1,K) = 0$, i.e., the energy is shifted in such a way that the interaction term is zero for a straight polymer. This leads to

$$\exp[g'(K)] = \int d\mathbf{t} \exp[2\,h(\mathbf{t}\cdot\mathbf{t}',K)]. \tag{11}$$

The recursions (10) and (11) are exact and can be used to obtain an exact RG relation for the eigenvalues $\lambda_k^{(N)}$ after N RG recursions,

$$\lambda_k^{(N+1)} = \left[\lambda_k^{(N)}\right]^2 \Big/ \left\{\sum_n^{(d)} \left[\lambda_n^{(N)}\right]^2\right\} = \left[\lambda_k^{(0)}\right]^{2^N} \Big/ \left\{\sum_n^{(d)} \left[\lambda_n^{(0)}\right]^{2^N}\right\}. \tag{12}$$

In general, the new and old interactions $h'(u,K)$ and $h(u,K)$ will differ in their functional structure. Thus the renormalization of the parameter K cannot be carried out in an exact and simple manner as for one-dimensional Ising-like models with discrete spin orientation [44]. The only fixed point function of the recursion (10) is independent of u, i.e., $h^*(u,K) = 0$ because of $h^*(1,K) = 0$. This result, together with the condition $h'(1,K) = 0$, which is imposed at every RG step, suggests that the function $h'(u,K)$ can be approximated by a *linear* function

$$h'(u,K) \simeq -K'(K)\,(1-u) \quad \text{for } u = \mathbf{t}\cdot\mathbf{t}'' \simeq 1, \tag{13}$$

as long as the scalar product $u = \mathbf{t}\cdot\mathbf{t}''$ is close to one, i.e., sufficiently close to the straight configuration. This approximation should improve when the whole function $h'(u,K)$ becomes small upon approaching the fixed point $h^*(u,K) = 0$ after many iterations, i.e., on large length scales. Using the approximation (13), $K'(K)$ is defined by the slope of $h'(u,K)$ at $u = 1$,

$$K'(K) \equiv \left.\frac{dh'(u,K)}{du}\right|_{u=1} = \left.\frac{d}{du}\exp\left[h'(u,K)\right]\right|_{u=1}, \quad \text{with } u = \mathbf{t}\cdot\mathbf{t}''. \tag{14}$$

Equivalently, one could expand the explicit expression for $h'(x,K)$ given by (10) and the right hand side of (13) for small tangent angles and compare the coefficients. In order to extract the renormalized bending rigidity κ' from the result for K', one has to take into

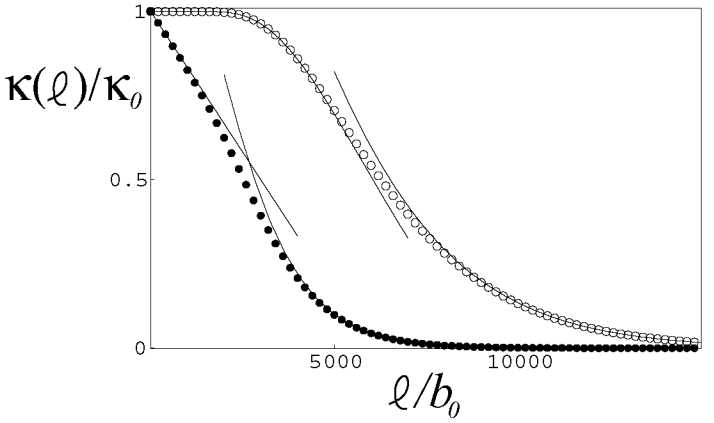

FIGURE 2. Renormalized bending rigidity $\kappa(\ell)/\kappa_0$ as a function of the length scale $\ell/b_0 = 2^N$ for small-scale bending rigidity $\kappa_0 = 1000 b_0 T$ ($K_0 = 1000$) in spatial dimension $d = 2$ ($\circ$) and $d = 3$ ($\bullet$) according to the recursion relation (16). The lines show the asymptotic behavior for $\ell \gg \kappa_0/T$ and $\ell \ll \kappa_0/T$ according to eqs. (17) and (19), respectively. Note that, in two dimensions, the renormalized bending rigidity remains essentially unchanged up to $\ell/b_0 \simeq \kappa_0/b_0 T$, see eq. (19).

account that K' also contains the new bond length $b' = 2b$, which increases by a factor of 2 at each decimation step. Therefore,

$$\kappa'(K) = 2bT\,K'(K). \tag{15}$$

Using this procedure we can calculate the renormalized bending rigidity κ_N after N RG recursions in two and three spatial dimensions starting from the exact RG recursions (12) for the eigenvalues. Inserting the renormalized eigenvalues into (7) or (8), taking the derivative according to (14) and applying the rescaling (15) finally yields the result

$$\frac{\kappa_N}{\kappa_0} = \frac{2^N}{K_0}\left\{\sum_n^{(d)}\left[\lambda_n^{(0)}(K_0)\right]^{2^N} A_n^{(d)}\right\}\Bigg/\left\{\sum_n^{(d)}\left[\lambda_n^{(0)}(K_0)\right]^{2^N}\right\}, \tag{16}$$

with $A_n^{(2)} \equiv n^2$ and $A_n^{(3)} \equiv \frac{1}{2}n(n+1)$. In the following we will interpret κ_N as a continuous function $\kappa(\ell)$ of the length scale ℓ by replacing the rescaling factor $2^N = b_N/b_0$ by the continuous parameter ℓ/b_0.

The sums in the expressions for the effective bending rigidity (16) can be computed numerically. Fig. 2 displays the results for $\kappa(\ell)/\kappa_0$ as a function of ℓ/b_0 for $K_0 = 1000$ and in two and three spatial dimensions. The value $K_0 = 1000$ is appropriate for a semiflexible polymer with $\kappa_0/T = 10\,\mu$m and a bond length $b_0 = 10$ nm, which is close to experimental values for F-actin [14, 15]. For DNA, appropriate values are $\kappa_0/T \simeq 50$ nm and $b_0 \simeq 0.3$ nm and, thus, $K_0 \simeq 150$.

As long as ℓ is small, κ decays almost linearly in $d = 3$, which is also in qualitative agreement with the result from the RG of the nonlinear σ-model. For $d = 2$ the decay is much slower at small length scales, but, in contrast to the non-linear σ-model where κ is

not renormalized. This qualitative difference is due to the following important difference between the Heisenberg and the nonlinear σ-model: Parametrizing the WLC model (2) via tangent angles leaves only quadratic terms $\propto (\Delta\theta_{i,i-1})^2$, whereas the discrete semiflexible chain (4) gives terms $\propto 1-\cos(\Delta\theta_{i,i-1})$, which represent the full expansion of the cosine and obey the local invariance under full rotations.

As ℓ increases $\kappa(\ell)$ approaches zero only asymptotically. Therefore, the definition of the persistence length as length scale where the renormalized κ vanishes, $\kappa(L_p)=0$ – which is usually used for fluid membranes – would always give an *infinite* result. We propose not to ask at which length scale the renormalized κ reaches zero, but rather *how* it reaches zero. For $\ell \geq b_0 K_0 = \kappa_0/T$ the sums in (16) converge fast and one has to include only the first few terms for accurate results. In fact, one can replace the Bessel functions contained in the eigenvalues $\lambda_k^{(0)}$, see (7) and (8), by their asymptotic form $I_k(x) \approx (x/2\pi)^{-1/2}\exp[x-(k^2-1/4)(2x)^{-1}]$ for large x [42]. This is justified for sufficiently large $K_0 \gtrsim 100$, which is fulfilled by semiflexible polymers like F-actin ($K_0 \simeq 1000$) or DNA ($K_0 \simeq 150$). Using this asymptotic we find $(\lambda_m^{(0)}(K_0))^{\ell/b_0} \sim e^{-m^2\ell/2b_0K_0}$ for $d=2$ and $(\lambda_l^{(0)}(K_0))^{\ell/b_0} \sim e^{-l(l+1)\ell/2b_0K_0}$ for $d=3$. Moreover, we may expand (16) as a power series in $e^{-\ell T/\kappa_0}$ and obtain

$$\begin{aligned} \kappa(\ell)/\kappa_0 &\approx (\ell T/\kappa_0)\left(2e^{-\ell T/2\kappa_0} - 4e^{-\ell T/\kappa_0} + 8e^{-3\ell T/2\kappa_0} - \ldots\right) \quad \text{for } d=2, \\ \kappa(\ell)/\kappa_0 &\approx (\ell T/\kappa_0)\left(3e^{-\ell T/\kappa_0} - 9e^{-2\ell T/\kappa_0} + 42e^{-3\ell T/\kappa_0} - \ldots\right) \quad \text{for } d=3\,. \end{aligned} \tag{17}$$

The characteristic length scales in the expansions are $2\kappa_0/T$ in $d=2$ and κ_0/T in $d=3$, which are, therefore, a natural definition for the persistence length L_p. For general dimensionality d, the exponent of the first term is determined by the order of the Bessel function appearing in the eigenvalue. Thus the RG calculation leads to a persistence length

$$L_p = \frac{2\kappa_0}{T(d-1)}, \tag{18}$$

which agrees exactly with the result (3) based on the tangent correlation function.

Our definition based on the large-scale asymptotics of the exact RG flow is qualitatively different from the definition used in perturbative RG calculations. While the result from the nonlinear σ-model is only valid for small length scales $\ell \ll \kappa_0/T$, where $\kappa(\ell)$ is close to κ_0, the expansions (17) describe the region $\ell \gg \kappa_0/T$. Indeed, taking the expansion of (16) for $\ell \ll \kappa_0/T$, that is

$$\begin{aligned} \kappa(\ell)/\kappa_0 &\approx 1-(8\pi^2\kappa_0/\ell T)e^{-2\pi^2\kappa_0/\ell T} + \mathcal{O}(\ell e^{-4\pi^2\kappa_0/\ell T}) \quad \text{for } d=2, \\ \kappa(\ell)/\kappa_0 &\approx 1-(\ell T/6\kappa_0) - \mathcal{O}(\ell^2T^2/\kappa_0^2) \quad \text{for } d=3, \end{aligned} \tag{19}$$

and defining L_p by the exponential decay length in two dimensions, respectively, by the linear term in three dimensions leads to a persistence length, which is considerably bigger than the value (18) found above. The slow exponential decay in the expansion (19) for $d=2$ is reminiscent of the non-renormalization of κ in the non-linear σ-model and leads to a "plateau" in the numerical result for $\kappa(\ell)/\kappa_0$ for $\ell \ll \kappa_0/T$ in Fig. 2.

In conclusion we have presented a definition of the persistence length L_p of a semiflexible polymer based on the large scale behavior of the RG flow of the bending rigidity κ, as obtained from a functional real-space RG calculation. Our result (18) for L_p generalizes the conventional definition based on the exponential decay of a particular two-point tangent correlation function and gives identical results for L_p, thus justifying past experimental and theoretical work based on this conventional definition. The RG flows (16) or (17) allow us to follow the behavior of a semiflexible polymer from a stiff polymer on short length scales to an effectively flexible polymer on large length scales quantitatively as a function of the length scale. On large length scales, our functional RG gives qualitatively different results from perturbative RG techniques, which have been used for the closely related problem of fluid membranes [35, 36, 37, 38, 39, 40] and which we also applied to the one-dimensional semiflexible polymer. The generalization of our renormalization approach to two-dimensional fluid membranes is complicated by the more involved differential geometry of these two-dimensional objects and remains an open issue for future investigation.

BUCKLING OF SEMIFLEXIBLE POLYMERS

Buckling of elastic rods is a ubiquitous mechanical problem, which is relevant in elasticity theory and mechanical engineering [4]. An elastic rod undergoes a buckling instability if the compressional force F exceeds a certain threshold value, the critical force F_c, for constant rod length or if the rod length L exceeds a certain critical length L_c for constant force. Such buckling instabilities also play a role in biological systems, whenever rigid filaments or semiflexible polymers, such as cytoskeletal filaments or DNA, are under a compressive load. In a living cell compressive loads can be generated by the polymerization of filaments or by molecular motors, both of which are driven by the hydrolysis of adenine triphosphate (ATP) [12]. Both processes can generate forces in the piconewton range. On the other hand, biological filaments also show pronounced thermal shape fluctuations, which should influence their buckling behavior.

It has been shown experimentally that polymerization forces are sufficient to buckle microtubules of micrometer length [23]. In Ref. [23], the shape of buckled microtubules growing against a hard obstacle has been analyzed to measure microtubule polymerization forces, which were found to lie in the piconewton range. Forces in the piconewton range can also be generated by motor proteins, and it has also been demonstrated experimentally that molecular motors can buckle microtubules of micrometer length [48]. Experiments on microtubules growing inside lipid vesicles demonstrate that microtubules also buckle under the compressive forces exerted by a lipid bilayer under tension [49].

All these experiments show that small forces in the piconewton range are sufficient to buckle cytoskeletal filaments. Such small buckling forces suggest that additional thermal forces, which also generate piconewton forces on a nanometer scale, could modify the buckling instability considerably. In this section we review our results on the influence of thermal fluctuations on the classical buckling instability in two spatial dimensions [47], which can be realized experimentally in confined geometries, i.e., for filaments adsorbed or confined to a planar substrate. We use a systematic expansion in the ratio L/L_p of contour length to persistence length, and integrate out small scale fluctuations to

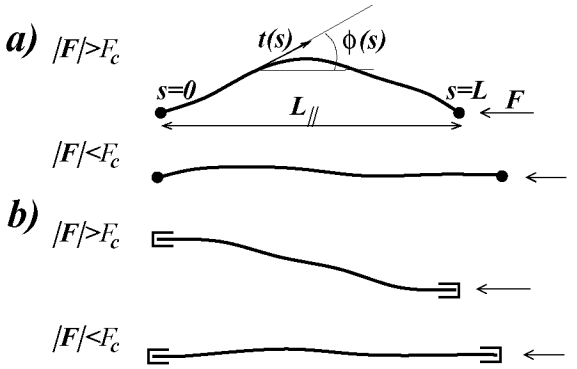

FIGURE 3. Thermally fluctuating filament under a compressive force $\mathbf{F}$ for (a) free and (b) clamped boundary conditions at both ends. If the absolute value $|\mathbf{F}|$ of the force exceeds the critical value F_c, the filament buckles; for $|\mathbf{F}| < F_c$ it remains unbuckled. The filament has contour length L, unit tangent vector $\mathbf{t}(s)$, and tangent angle $\phi(s)$ at arc length s. The parameter $L_\parallel$ is the projected length in the force direction.

obtain an effective theory governing the buckling instability in the presence of thermal fluctuations. This leads to a shift of the buckling force in the presence of thermal fluctuations, and we find that the buckling force *increases* in two dimensions. We also calculate the mean projected length as a function of the applied force (at fixed contour length) and as a function of the contour length (at fixed applied force) in the presence of thermal fluctuations, and our results show that thermal fluctuations lead to a *stretching* of buckled filaments, whereas they compress unbuckled filaments.

To describe a semiflexible polymer under a compressive force in two spatial dimensions we use the worm-like chain Hamiltonian (2) and fulfill the constraint $|\mathbf{t}(s)| = 1$ explicitly by using a parametrization in terms of the tangent angle $\phi(s)$, i.e., $\mathbf{t}(s) = (\cos\phi(s), \sin\phi(s))$. The Hamiltonian also contains an additional energy contribution from the compressive force and becomes

$$\mathscr{H} = \int_0^L ds \left[\frac{\kappa}{2} (\partial_s \phi)^2 + F \cos\phi(s) \right], \tag{20}$$

where $F \equiv |\mathbf{F}|$ is the absolute value of the compressive force. We consider the buckling instability of the straight state $\phi(s) = 0$ and the compressive force is acting in the direction $\phi = \pi$. An important quantity, which can serve as an order parameter for the buckling instability, is the projected length $L_\parallel$, which is given by

$$L_\parallel = \int_0^L ds \cos\phi(s). \tag{21}$$

Buckling at zero temperature

The classical buckling instability is obtained by minimizing the total energy (20) with respect to the angle configuration $\phi(s)$. This minimization leads to the beam equation

$$\kappa\partial_s^2\phi + F\sin\phi(s) = 0 \tag{22}$$

which has to be solved for appropriate boundary conditions. Boundary conditions at each end of the rod can be classified as free or clamped, where "free" means that the tangent at the end point can freely adapt to the compressional force and "clamped" means that it is constrained to a certain direction, which is usually parallel to the applied force. In the following, we will focus on boundary conditions with two clamped or two free ends. In two dimensions, as considered here, we use either clamped boundary conditions $\phi(0) = \phi(L) = 0$ with both tangent vectors (anti-)parallel to the applied force or free boundary conditions, which correspond to $\partial_s\phi(0) = \partial_s\phi(0) = 0$, i.e., a vanishing curvature and thus a vanishing torque at the filament ends.

Solving the beam equation (22) one finds that a non-zero buckled solution exists at zero temperature above a critical buckling force $F_{c,0}$, which is given by

$$F_{c,0} = \pi^2\kappa/L^2 \tag{23}$$

both for free and clamped ends and fixed contour length L. Alternatively, if the filament polymerizes against a fixed compressive load F, it will buckle above a critical contour length

$$L_{c,0} = \pi\left(\kappa/F\right)^{1/2} \tag{24}$$

at zero temperature.

Energy minimization gives the contour length L as well as the projected length $L_\parallel$ as a function of the maximal buckling angle ϕ^*, which is attained at $s = 0$ or $s = L$ for two free ends and for $s = L/2$ for two clamped ends,

$$\frac{L}{L_{c,0}} = \sqrt{\frac{F}{F_{c,0}}} = \frac{\mathscr{I}_1(\phi^*)}{\mathscr{I}_1(0)}, \tag{25}$$

$$\frac{L_\parallel}{L_{c,0}} = \frac{\mathscr{I}_1(\phi^*) - \mathscr{I}_2(\phi^*)}{\mathscr{I}_1(0)} \tag{26}$$

with the two integrals

$$\mathscr{I}_1(y) \equiv \int_0^y dx \frac{1}{\sqrt{2(\cos x - \cos y)}} \quad \text{and} \quad \mathscr{I}_2(y) \equiv \int_0^y dx \frac{1-\cos x}{\sqrt{2(\cos x - \cos y)}}. \tag{27}$$

As y goes to zero, the first integral has the finite limit $\mathscr{I}_1(0) = \pi/2$ whereas $\mathscr{I}_2(0) = 0$. Relations (25) and (26) can also be used as implicit equations to determine the buckling angle ϕ^* for given contour length L or projected length $L_\parallel$, respectively.

Using the Eqs. (25) and (26), one can obtain parametric representations of the reduced projected length $L_\parallel/L$ or $L_\parallel/L_{c,0}$ as a function of the reduced force or the reduced contour length

$$\bar{F} \equiv F/F_{c,0} \quad \text{and} \quad \bar{L} \equiv L/L_{c,0}, \tag{28}$$

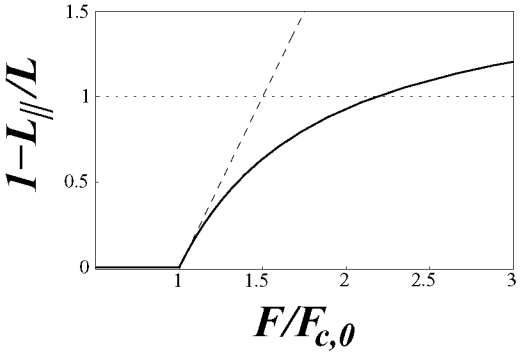

FIGURE 4. Reduced and shifter projected length $1 - L_{\|}/L$ as a function of the reduced force $F/F_{c,0}$ with the critical buckling force $F_{c,0}$ as given by (23). For $F < F_{c,0}$, the filament is straight with $L_{\|} = L$ and $1 - L_{\|}/L = 0$. The buckled solution appears for $F > F_{c,0}$. The solid curve is obtained numerically from relations (25) and (26) by a parametric plot using the buckling angle ϕ^* as the curve parameter. The dashed line is the linear approximation (29). For $F/F_{c,0} > 2.183$, the projected length $L_{\|}$ becomes negative.

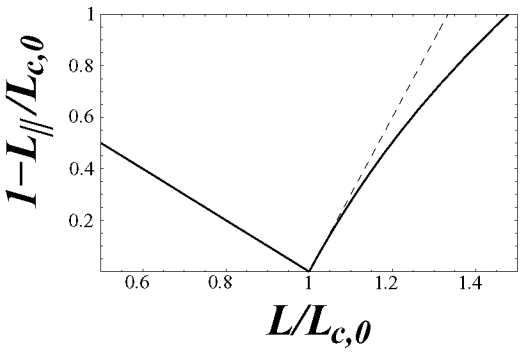

FIGURE 5. Reduced and shifted projected length $L_{\|}/L_{c,0}$ as a function of the reduced contour length $L/L_{c,0}$ with the critical contour length $L_{c,0}$ as given by (24). For $L < L_{c,0}$, the filament is straight with $L_{\|} = L$ which corresponds to the left part of the diagram with $L/L_{c,0} < 1$. The buckled solution appears for $L > L_{c,0}$. The solid curve is obtained numerically by a parametric plot using the buckling angle ϕ^* as the curve parameter in eqs. (25) and (26). The dashed line is the linear approximation (29). For $L/L_{c,0} > 1.478$, the projected length $L_{\|}$ becomes negative.

in the buckled state with $F > F_{c,0}$ or $L > L_{c,0}$, see Figs. 4 and 5, where we use the buckling angle ϕ^* as a curve parameter. Close to the buckling instability we find the asymptotic behavior

$$\begin{aligned} 1 - L_{\|}/L &\approx 2\,(\bar{F} - 1) \text{ for small } \bar{F} - 1 > 0, \\ 1 - L_{\|}/L_{c,0} &\approx 3\,(\bar{L} - 1) \text{ for small } \bar{L} - 1 > 0. \end{aligned} \tag{29}$$

For $L < L_{c,0}$, on the other hand, the filament is unbuckled which implies that the projected length $L_\parallel$ is identical with the contour length L and

$$1 - L_\parallel / L_{c,0} = 1 - \bar{L} \text{ for } \bar{L} - 1 < 0. \tag{30}$$

Combining the two results for $L > L_{c,0}$ and $L < L_{c,0}$, we see that the relation between projected and contour length exhibits a cusp at the buckling point with $L = L_{c,0}$ [50], as shown in Fig. 5. The cusp could be used to detect the buckling threshold in experiments on growing filaments under a fixed compressive load, which could be generated, for example, by optical traps. The parametric representations shown in Figs. 4 and 5 and thus the asymptotic behavior (29) just above the buckling threshold are valid both for two free and two clamped ends.

Buckling in the presence of thermal fluctuations

In order to consider the effects of thermal fluctuations on the buckling instability, several approaches are possible. We can expand around the "classical" configuration obtained in the previous section and integrate out fluctuations up to quadratic (or higher) order. This approach, however, does not allow us to calculate a fluctuation-induced shift of the threshold force for buckling. Therefore we employ a renormalization-like procedure where we integrate out short wavelength fluctuations in order to obtain an effective theory governing the long wavelength buckling instability. We focus on the regime close to the buckling instability where we can expand the Hamiltonian (20) in tangent angles up to quartic order, and obtain

$$\mathscr{H} = \int_0^L ds \left[\frac{\kappa}{2} (\partial_s \phi)^2 + F \left(1 - \frac{1}{2}\phi^2(s) + \frac{1}{24}\phi^4(s) \right) \right]. \tag{31}$$

For free and clamped boundary conditions, Fourier expansion of $\phi(s)$ leads to

$$\phi(s) = \sum_{n=1}^{N} \tilde{\phi}_n \cos(n\pi s/L) \quad \text{(free)}, \tag{32}$$

$$\phi(s) = \sum_{n=1}^{N} \tilde{\phi}_n \sin(n\pi s/L) \quad \text{(clamped)}, \tag{33}$$

respectively, with Fourier coefficients $\tilde{\phi}_n$. The maximal wave number N is given by the number of degrees of freedom, $N = L/a$, where a is a microscopic cutoff, which is set by the monomer size or the filament diameter. The $n = 0$ mode is absent for free boundary conditions because we apply the additional constraint $z(L) - z(0) = \int_0^L ds \sin\phi(s) = 0$ that the end points have the same height coordinate (perpendicular to the force direction). This constraint is automatically fulfilled by the zero temperature solution but has to be imposed separately in the presence of thermal fluctuations. The condition $\tilde{\phi}_0 = 0$ satisfies this constraint up to terms of order $\mathscr{O}(\tilde{\phi}_n^3)$.

In order to investigate the effect of the anharmonic quartic terms, we write the Hamiltonian (31) as

$$\mathscr{H} = \mathscr{H}_2 + \mathscr{H}_4, \tag{34}$$

where $\mathscr{H}_2$ contains all terms up to quadratic order and $\mathscr{H}_4$ the remaining terms up to quartic order. Using the Fourier expansions (32) or (33), the quadratic part can be rewritten as

$$\mathscr{H}_2\{\tilde{\phi}_n\} \;=\; FL + \sum_{n\geq 1} \frac{F_{c,0}L}{4}\left(n^2 - \bar{F}\right)\tilde{\phi}_n^2. \tag{35}$$

This representation in Fourier modes shows that buckling is an instability of the $n = 1$ mode for $\bar{F} > 1$, which attains a non-zero equilibrium value in this regime at zero temperature. Higher modes $n > 1$ remain stable up to higher order buckling forces, i.e., for $\bar{F} < n^2$. In the following we focus on the regime $\bar{F} \ll 4$, where only the $n = 1$ mode can become unstable and large. Expectation values for higher modes $n, m \geq 2$,

$$\langle \tilde{\phi}_n \tilde{\phi}_m \rangle = \delta_{nm} \frac{2T}{F_{c,0}L} \frac{1}{n^2 - \bar{F}}, \tag{36}$$

as calculated with the Hamiltonian (35) are of the order of

$$\frac{T}{F_{c,0}L} = \frac{1}{\pi^2}\frac{L}{L_p} \equiv t. \tag{37}$$

The dimensionless parameter t is a reduced temperature, which is small for semiflexible filaments with $L \lesssim L_p$. Expectation values $\langle \tilde{\phi}_n^2 \rangle \sim t$ of higher modes are thus small as well. The parameter t will be used in the following as an expansion parameter for the systematic treatment of fluctuations. This parameter is small in the limit of small temperature, large bending rigidity, or small contour length. A typical value for a microtubule of contour length $L = 10\mu$m and $L_p = 1$mm is $t \simeq 10^{-3}$, whereas an actin filament of contour length $L = 10\mu$m and $L_p = 15\mu$m has a much larger value $t \simeq 6.7 \times 10^{-2}$.

This motivates our treatment of the quartic Hamiltonian $\mathscr{H}_4$. Because fluctuations of higher Fourier modes $n \geq 2$ will remain small at the buckling transition, we neglect terms of cubic and quartic order in the Fourier modes $n \geq 2$. The corresponding terms for the unstable $n = 1$ mode have to be retained, and we obtain

$$\mathscr{H}_4\{\tilde{\phi}_n\}/T = \frac{\bar{F}}{64t}\tilde{\phi}_1^4 \pm \frac{\bar{F}}{48t}\tilde{\phi}_1^3\tilde{\phi}_3 + \sum_{n\geq 2}\frac{\bar{F}}{16t}\left(\tilde{\phi}_1^2\tilde{\phi}_n^2 \pm \tilde{\phi}_1^2\tilde{\phi}_n\tilde{\phi}_{n+2}\right). \tag{38}$$

The upper and lower signs in Eq. (38) are for free and clamped boundary conditions, respectively.

We first trace over all higher order modes $n \geq 2$ in order to obtain an effective Hamiltonian for the single mode $n = 1$, which is the relevant mode for the buckling instability.

$$e^{-\mathscr{H}_{\rm eff}\{\tilde{\phi}_1\}/T} = \left(\prod_{n\geq 2}\int_{-\infty}^{\infty} d\tilde{\phi}_n\right) e^{-\mathscr{H}_2\{\tilde{\phi}_n\}/T - \mathscr{H}_4\{\tilde{\phi}_n\}/T}. \tag{39}$$

The Hamiltonian $\mathscr{H}_2 + \mathscr{H}_4$, as given by Eqs. (35) and (38), is quadratic in the higher order modes and the Gaussian integrals in Eq. (39) can be performed to obtain

$$\mathscr{H}_{\text{eff}}\{\tilde{\phi}_1\}/T = \bar{F}/t + \alpha\tilde{\phi}_1^2 + \beta\tilde{\phi}_1^4 \tag{40}$$

with

$$\alpha \equiv \frac{1}{4}\left(\frac{1-\bar{F}}{t} + \frac{1}{2}h(\bar{F})\right), \tag{41}$$

$$h(\bar{F}) \equiv \sum_{n\geq 2}\frac{\bar{F}}{n^2-\bar{F}}, \tag{42}$$

$$\beta \equiv \frac{1}{64}\frac{\bar{F}}{t} \tag{43}$$

to leading order in the small parameter t. We point out that up to this order there is no difference between clamped and free boundary conditions. Therefore, our results regarding the critical force and the mean projected length will be identical for both types of boundary conditions also in the presence of thermal fluctuations. The function $h(\bar{F})$ can be approximated by $h(\bar{F}) \simeq \sqrt{\bar{F}}\,\text{arccoth}\left(2/\sqrt{\bar{F}}\right)$ by converting the sum into an integral. Close to the buckling threshold around $\bar{F} = 1$ we can also find an exact expression for the Taylor expansion $h(\bar{F}) \approx 3/4 + (1-\bar{F})(\pi^2/12 + 1/16)$. For $t \ll 1$ we can therefore use

$$\alpha \approx \frac{1}{4}\left(\frac{3}{8} + \frac{1-\bar{F}}{t}\right) \tag{44}$$

to a good approximation.

The resulting effective theory (40) for the single mode $\tilde{\phi}_1$ is a fourth order Ginzburg-Landau-type theory. The buckling instability occurs if the coefficient $\alpha(\bar{F})$ of the quadratic term changes sign. This determines the critical force F_c in the presence of thermal fluctuations,

$$F_c = F_{c,0}\left(1 + \frac{t}{2}h(\bar{F}_c)\right) \approx F_{c,0}\left(1 + \frac{3t}{8}\right) \tag{45}$$

where the last approximation is to leading order in the reduced temperature t such that $h(\bar{F}_c) \approx h(1) = 3/4$. Using the relation $\bar{F} = \bar{L}^2$, we obtain the corresponding result for the critical contour length L_c in the presence of thermal fluctuations,

$$\bar{L}_c = \sqrt{\bar{F}_c} \approx 1 + \frac{3t}{16} \tag{46}$$

to leading order in t. It is remarkable that, in two dimensions as considered here, the critical buckling force *increases* because of fluctuation effects as described by eq. (45). In the special case of two dimensions, the short wavelength fluctuations always *weaken* the effect of the applied force on a larger scale because the fourth order contribution to the force term in the Hamiltonian (31) has a sign opposite to the leading quadratic contribution. On the other hand, it is well known that short wavelength fluctuations do

not affect the bending rigidity on a larger scale in two dimensions because there is no bending rigidity renormalization in two dimensions for the continuous worm-like chain model (20) according to the results of the previous section. The combination of these two effects leads to the increase of the critical buckling force in the presence of thermal fluctuations.

For arbitrary spatial dimensions d, a more general argument based on the RG flow of the nonlinear σ model is given in Ref. [47] and suggests that thermal fluctuations increase the buckling force for dimensions $d < 3$, whereas they decrease the buckling force for dimensions $d > 3$.

The partition sum Z is obtained by performing the one-dimensional integral over the remaining Fourier amplitude mode $\tilde{\phi}_1$,

$$Z = \int_{-\infty}^{\infty} d\tilde{\phi}_1 e^{-\mathscr{H}_{\rm eff}\{\tilde{\phi}_1\}/T}. \tag{47}$$

From the force dependence of the partition sum the mean value of the projected filament length $L_\parallel$ from eq. (21) can be determined from the relation

$$\langle L_\parallel \rangle = -T\,\partial_F \ln Z(F). \tag{48}$$

Performing this calculation we finally obtain

$$1 - \frac{\langle L_\parallel \rangle}{L} = -\frac{t}{4\bar{F}} - \mathscr{F}_1\left(\frac{\alpha}{\beta^{1/2}}\right)\frac{t^{1/2}}{\bar{F}^{3/2}}\,(\bar{F}_c + \bar{F}) \tag{49}$$

with

$$\frac{\alpha}{\beta^{1/2}} \approx \frac{2}{t^{1/2}\bar{F}^{1/2}}\,(\bar{F}_c - \bar{F})\,, \tag{50}$$

where

$$\mathscr{F}_1(y) \equiv \begin{cases} \dfrac{\mathscr{F}'(y)}{\mathscr{F}(y)} = \dfrac{y}{4}\left(1 - \dfrac{\mathrm{K}_{3/4}(y^2/8)}{\mathrm{K}_{1/4}(y^2/8)}\right) & \text{for } y > 0, \\ \dfrac{y}{4}\left(1 + \dfrac{\mathrm{I}_{3/4}(y^2/8) + \mathrm{I}_{-3/4}(y^2/8)}{\mathrm{I}_{1/4}(y^2/8) + \mathrm{I}_{-1/4}(y^2/8)}\right) & \text{for } y < 0 \end{cases} \tag{51}$$

is a monotonously increasing, negative function. The solid curves in Fig. 6a show the result (49) for $1 - \langle L_\parallel \rangle / L$ as a function of the reduced force $\bar{F}$ for different values of the parameter t.

Further analysis of the result (49) in the vicinity of the buckling threshold reveals an interesting behavior: Thermal fluctuations as described by the small parameter t *decrease* the mean projected length $\langle L_\parallel \rangle$ below its zero temperature value $L_\parallel = L$ for $\bar{F} < \bar{F}_c$ whereas they *increase* the mean projected length above the zero temperature value $L_\parallel = L\bar{F}^{-2}$ in the buckled state for $\bar{F} > \bar{F}_c$. We thus conclude that thermal fluctuations lead to a stretching of buckled filaments, whereas they compress unbuckled ones. This implies that two curves for the mean projected length $\langle L_\parallel \rangle$ as a function of force, which are taken at different temperatures t, should *intersect* in the vicinity of the

buckling force. This characteristic behavior is clearly confirmed in Figs. 6a, where the full analytical result (49) is shown at different temperatures.

A characteristic feature of the buckling instability at zero temperature is the cusp in the relation between projected and contour length at the critical contour length $L_{c,0}$, see Fig. 5. For $L < L_{c,0}$ in the unbuckled state, the projected length is given by $L_\parallel = L$ and grows with the contour length. The projected length becomes maximal at the critical length $L = L_{c,0}$, where the filament buckles. If the filament grows further after buckling, $L > L_{c,0}$, the projected length decreases and $L_\parallel < L_{c,0}$. In the presence of thermal fluctuations, the cusp becomes modified, and we obtain the reduced mean projected length $1 - \langle L_\parallel \rangle / L_{c,0}$ as a function of the reduced contour length $\bar{L}$ by applying the relations $\bar{F} = \bar{L}^2$ and

$$1 - \frac{\langle L_\parallel \rangle}{L_{c,0}} = \left(1 - \frac{\langle L_\parallel \rangle}{L}\right) \bar{L} + (1 - \bar{L}) \tag{52}$$

to our previous result (49). This gives

$$1 - \frac{\langle L_\parallel \rangle}{L_{c,0}} = 1 - \bar{L} - \frac{t}{4\bar{L}} - \mathscr{F}_1\left(\frac{\alpha}{\beta^{1/2}}\right) \frac{t^{1/2}}{\bar{L}^2} \left[\bar{L}_c^2 + \bar{L}^2\right] \tag{53}$$

with

$$\frac{\alpha}{\beta^{1/2}} \approx \frac{2}{t^{1/2}\bar{L}} \left[\bar{L}_c^2 - \bar{L}^2\right]. \tag{54}$$

The solid curves in Fig. 6b represent the expression $1 - \langle L_\parallel \rangle / L_{c,0}$ as a function of $\bar{L}$ according to eq. (53). Thermal fluctuations lead to a rounding of the zero temperature cusp to a pronounced minimum and to a shift of the location $\bar{L}_m$ of this minimum. Because thermal fluctuations lead to a stretching of buckled filaments, whereas they compress unbuckled filaments, curves for different temperatures t *intersect* in Fig. 6b, In principle, the contour length $\bar{L}_m$, where the mean projected length $\langle L_\parallel \rangle$ is maximal, could be determined experimentally by observing filaments growing against an obstacle as in Ref. [23].

In order to check our analytical predictions, we perform Monte Carlo simulations of buckling filaments in two dimensions in the presence of thermal fluctuations. We simulate a discretized version of the Hamiltonian (20) and employ clamped boundary conditions. In order to equilibrate the filament, we use two kinds of Monte Carlo (MC) moves: (i) a local move in real space, which changes the angles of two neighboring segments in opposite directions and thus induces a displacement of the point connecting both segments in the direction perpendicular to the local filament orientation; (ii) a collective move in Fourier space, which changes the amplitude $\tilde{\phi}_n$ of Fourier mode n by a random amount. For the simulation results shown in Figs. 6, we used a discretization into $N = 200$ segments and performed 8×10^6 MC sweeps alternating local moves and moves in Fourier space.

The simulation results for the reduced projected length $\langle L_\parallel \rangle / L$ as a function of the reduced force $\bar{F}$ in Fig. 6a are in good agreement with our analytical result (49). Deviations become appreciable for the largest values of the reduced temperature $t \simeq 10^{-1}$ for which we performed simulations. For these values it becomes necessary to

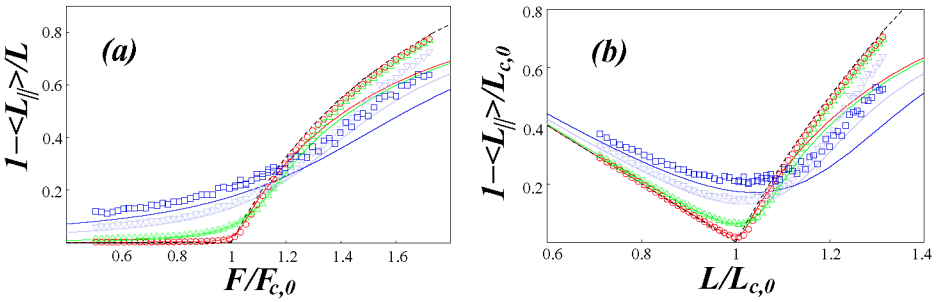

FIGURE 6. Monte Carlo simulation data for the reduced and shifted projected length $1 - \langle L_{\|} \rangle / L_{c,0}$ as a function of (a) the reduced force $F/F_{c,0}$ and (b) the reduced contour length $L/L_{c,0}$. The two ends of the filament are clamped using the model (20) for reduced persistence lengths $L_p/L = 100$ (red, $\circ$), 10 (green, $\triangle$), 2 (light blue, $\triangledown$), and 1 (blue, $\square$) corresponding to reduced temperatures $t \simeq 10^{-3}, 10^{-2}, 5 \times 10^{-2}$, and 10^{-1} with t as defined in (37). The solid lines show the analytic results (49) and (53). The analytical zero temperature solutions from Figs. 4 and 5 are shown as a dashed line.

include higher order terms in the expansion in t underlying the analytical result (49). In particular, also the MC simulations confirm that curves for the mean projected length $\langle L_{\|} \rangle$ as a function of force, taken at different temperatures t, *intersect* in the vicinity of the buckling force. Also the MC results for the reduced projected length $\langle L_{\|} \rangle / L_{c,0}$ as a function of the reduced contour length $\bar{L}$ in Fig. 6b are in good agreement with the analytical result (53). The existence of a cusp rounded by thermal fluctuations close to the critical length L_c is clearly confirmed.

In conclusion, we presented in this section a systematic study of the buckling instability in the presence of thermal fluctuations in two spatial dimensions. By integrating over all short wavelength modes we derived an effective theory governing the buckling instability of the Fourier mode with the longest wavelength given by the filament length. We find that thermal fluctuations *increase* the critical force for buckling in two spatial dimensions. The increase in the critical buckling force is closely related to our main result that curves for the mean projected length $\langle L_{\|} \rangle$ measuring the end-to-end extension of the filament as a function of the applied compressive force, which are taken at different temperatures, *intersect* in the vicinity of the buckling force. This leads to the conclusion that, in two spatial dimensions, thermal fluctuations lead to a stretching of buckled filaments, whereas they compress unbuckled filaments. Before buckling a filament is governed by entropy and an increasing temperature leads to a shortening of the filament in order to maximize its configurational entropy, similar to the well-known elastic behavior of a flexible polymer, which gives rise to classical rubber elasticity [51]. A buckled filament, on the other hand, is governed by its bending energy and for increasing temperature also the bending energy decreases in favor of the entropy, which gives rise to the observed effect of stretching by thermal fluctuations.

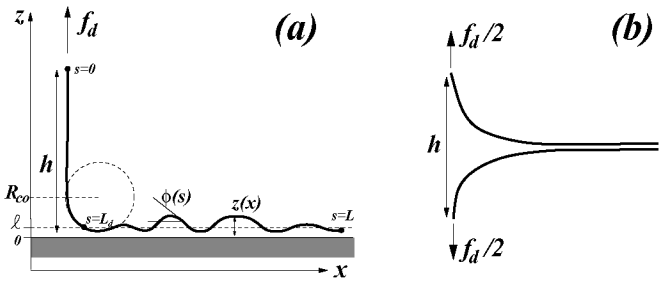

FIGURE 7. Force-induced desorption (a) and unzipping (b) of semiflexible polymers; f_d is the desorbing or unzipping force and h the height or separation of the end points.

ADSORPTION AND DESORPTION

In this section we want to consider the problem of peeling a single adhesive semiflexible polymer or filament from a surface, which is closely related to the problem of separating two adhesive filaments [52]. Over the past decade, experimental force spectroscopy techniques such as atomic force microscopy (AFM), optical or magnetic tweezers have been developed, which allow to perform manipulation experiments on individual polymers with spatial resolution in the nanometer range and force resolution in the piconewton range, for example, the mechanical unfolding of single proteins [53], the stretching of single DNA [54, 55]. Particularly suited for such single polymer manipulation experiments are semiflexible polymers with a high molecular weight per monomer and a large diameter. The quantitative analysis of force spectroscopy on semiflexible polymers requires theoretical models that take into account the combined effects of external force, temperature, and polymer bending energy. In this section we discuss results from theory and simulation for the force-induced desorption of semiflexible polymers. We will first discuss force-induced desorption at zero temperature, which is a variational or mechanical problem. Then we point out corrections from thermal fluctuations. Force-induced desorption experiments with single semiflexible polymers have been realized experimentally by attaching adsorbed polyelectrolytes to an AFM tip [56, 57, 58, 26, 59, 60]. The most recent experiments [26, 59, 60] give access to the single polymer force-distance curve. Force-induced desorption is assisted by thermal fluctuations and, thus, also gives additional insight into the fundamental problem of the adsorption transition of semiflexible polymers, which has been studied intensively both analytically [61, 62, 63, 64, 65, 66, 67, 68, 69, 70] and by simulations [71, 72].

Force-induced desorption at zero temperature

In the absence of thermal fluctuations ($T = 0$), a semiflexible polymer is only governed by its bending energy, and we recover a classical mechanics problem similar to fracture. At $T = 0$, polymer excursions parallel to the adhesive surface are suppressed, and the configuration of a polymer segment of contour length L can be pa-

rameterized by tangent angles $\phi(s)$ with respect to the adhesive surface, where s is the arc length ($0 < s < L$), see Fig. 7. The bending energy is given by the Hamiltonian $E_b = (\kappa/2)\int_0^L ds(\partial_s\phi)^2$, which is the same representation as in eq. (20). The adsorption energy is

$$E_a = \int_0^{L_c} ds V(z(s)), \tag{55}$$

where $z(s)$ is the distance of polymer segments from the adsorbing surface at $z = 0$ and $V(z)$ is a generic square well adhesion potential of small range ℓ with $V(z) = W < 0$ for $z < \ell$, $V(z) = 0$ for $z > \ell$, and $V(z) = \infty$ for $z < 0$ due to the hard wall. For van der Waals forces or screened electrostatic interactions the potential range ℓ is comparable to the polymer thickness or the Debye-Hückel screening length, respectively. For the discussion at $T = 0$, we consider a contact potential, i.e., the limit of small ℓ. In the absence of a desorbing force the polymer lies flat on the adhesive surface [$\phi(s) = 0$ for all s] gaining an energy $-|W|L$. The semiflexible polymer is peeled from the adhesive surface by a localized desorbing force $\mathbf{f}_d$ that is applied in z-direction at the end point $s = 0$. Under the influence of the force, a polymer segment $0 < s < L_d$ desorbs, which costs a potential energy $|W|L_d$. In order to map out the energy landscape of the desorption process, we consider a *constrained* equilibrium and minimize the sum of bending and potential energy of the polymer, $E = |W|(L_d - L_c) + E_b$, under the constraint of a fixed height $h = \int_0^{L_d} ds \sin\phi(s)$ of the polymer end at $s = 0$. Minimizing with respect to L_d gives the transversality condition $\partial_s\phi(L_d) = -(2|W|/\kappa)^{1/2} \equiv 1/R_{co}$ which determines the contact curvature radius R_{co} [73]; the boundary conditions are $\phi(L_d) = 0$ and $\partial_s\phi(0) = 0$ corresponding to a free tangent. Solving the shape equation in the presence of the height constraint, we find the scaling form $\Delta E(h) \equiv E(h) - E(0) = (\kappa|W|)^{1/2}\mathscr{F}_E(h/R_{co})$ for the total energy with the two limits

$$\Delta E(h) \approx \begin{cases} 2^{7/4}3^{-1/2}h^{1/2}\kappa^{1/4}|W|^{3/4} & \text{for } h \ll R_{co} \\ |W|[h + 4(\sqrt{2}-1)R_{co}] & \text{for } h \gg R_{co} \end{cases}. \tag{56}$$

For the desorbed polymer length we obtain the scaling result $L_d(h) = R_{co}\mathscr{F}_L(h/R_{co})$ with the limits

$$L_d \approx \begin{cases} \sqrt{3}h^{1/2}R_{co}^{1/2} & \text{for } h \ll R_{co} \\ h + 2(\sqrt{2}-1)R_{co} & \text{for } h \gg R_{co} \end{cases}. \tag{57}$$

The results (56) and (57) can be corroborated by a scaling argument starting from the estimate $\Delta E(h, L_d) \sim \kappa h^2/L_d^3 + |W|L_d$ of the energy cost to desorb a segment of length L_d. For $h \ll R_{co}$, energy minimization with respect to the desorbed length L_d gives $L_d \sim h^{1/2}\kappa^{1/4}|W|^{-1/4}$ and an energy cost $\propto h^{1/2}$ as in (56). For $h \gg R_{co}$ essentially the whole desorbed length L_d is lifted straight and perpendicular to the substrate except for a curved segment of length $\sim R_{co}$ around the contact point, which leads to $L_d \approx h + \mathscr{O}(R_{co})$ and an energy cost $\propto h$ as in (56).

Including the energy gain for a constant desorbing force f_d, we obtain the energy landscape $\Delta G(h) \equiv \Delta E(h) - f_d h$ at $T = 0$ as a function the height h, see Fig. 8b. The equilibrium height minimizes $\Delta G(h)$, and we find a first order desorption transition from $h = 0$ to infinite h above the critical force $f_{d,c} = |W|$. For *all* force values $f_d > |W|$,

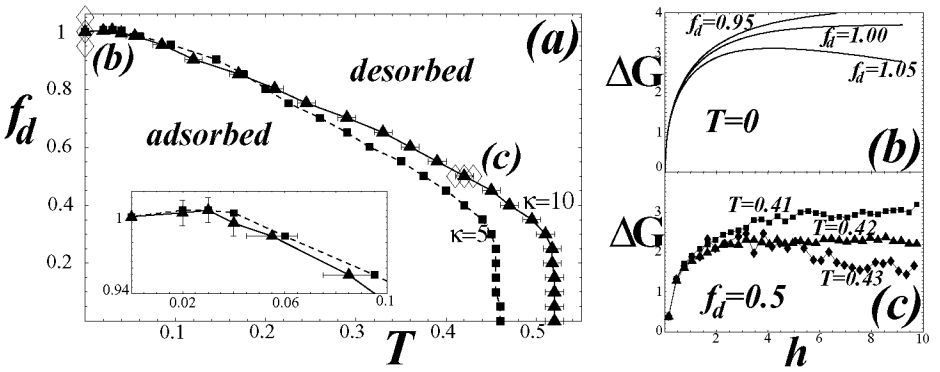

FIGURE 8. (a) Phase diagrams in the plane of the desorbing force f_d and temperature T from Monte Carlo simulations of a discretized semiflexible chain (with segments of length Δs) and bending rigidities $\kappa = 10$ (triangles) and $\bar{\kappa} = 5$ (squares), adsorption potential range $\ell = 0.1$, and contour length $L_c = 100$ (lengths ℓ and L_c in units of Δs, temperature T in units of the adhesion energy $|W|\Delta s$, desorbing force f_d in units of $|W|$, and bending rigidities κ in units of $|W|\Delta s^2$). Lines are guides to the eye. The inset shows the reentrance region at low temperatures. (b),(c) Free energy landscapes $\Delta G(h)$ as a function of the height h for $\kappa = 10$ and forces and temperatures as indicated by diamonds in the phase diagram b. (b) at $T = 0$ according to the analytical result, see eq. (56). (c) for $f_d = 0.5$ from Monte Carlo simulations in agreement with eqs. (60) and (61). In the desorbed phase $\Delta G(h)$ exhibits an energy barrier.

there remains a local minimum at $h = 0$ corresponding to the firmly adsorbed state, which is separated by an *energy barrier* ΔG_b from the desorbed equilibrium state. The energy barrier is given by $\Delta G_b \approx 2^{3/2}\kappa^{1/2}|W|^{3/2}/3f_d$ for all $f_d > |W|$, i.e., it decays as $1/f_d$ and scales with $\kappa^{1/2}$ and, hence, is a consequence of the bending rigidity of the polymer. The scaling behavior of ΔG_b also follows from equating the energy cost $\Delta E(h) \propto h^{1/2}\kappa^{1/4}|W|^{3/4}$ and the gain $f_d h$. Due to the energy barrier, force-induced desorption requires thermal activation or an h-dependent force $f_d(h) = \partial_h \Delta E(h)$, which diverges as $h^{-1/2}$ for small h.

Force-induced desorption in the presence of thermal fluctuations

In the absence of a desorbing force ($f_d = 0$), a semiflexible polymer can undergo thermal desorption [69, 70]. In order to discuss the influence of thermal fluctuations onto the force-induced desorption we first give some basic results on the thermal desorption transition in the absence of an additional force. Using a model connecting length scales below and above the persistence length L_p. At the desorption transition, the correlation length $\xi_\parallel$ diverges. For $\xi_\parallel < L_p$, we apply results for a weakly bent *semiflexible* polymer [69], whereas we use standard results for the adsorption of *flexible* Gaussian polymers in combination with an effective adsorption potential for $\xi_\parallel > L_p$. In the latter flexible regime, desorbed segments of typical length $\xi_\parallel$ decay into uncorrelated persistent Kuhn segments of length $\sim L_p$. The strength of the effective renormalized adsorption potential for these Kuhn segments is given by the free energy of adsorption $f_{W,\mathrm{SF}}$

of a semiflexible segment. This construction connects the semiflexible and the flexible regime. Using this approach we find the for critical potential strength for desorption, $W_c \approx -\frac{\sqrt{3\pi}}{2^{4/3}}(T/\ell^{2/3}L_p^{1/3})[1+\frac{\pi^{3/2}}{2^{8/3}3^{3/2}}(\ell/L_p)^{2/3}]$, and a free energy of adsorption

$$|f_W| \approx \begin{cases} 3(W-W_c)^2 L_p/2T & \text{for } |W-W_c| \ll T/L_p \\ |f_{W,\mathrm{SF}}| \sim |W-W_c| & \text{for } |W-W_c| \gtrsim T/L_p \end{cases}, \tag{58}$$

which is related to the correlation length by $|f_W| = T/\xi_\parallel$. The first line in (58) is the free energy of adsorption in the flexible regime; the second line is the free energy of adsorption in the semiflexible regime, which holds for $|f_W| \gtrsim T/L_p$ or outside a window of adhesion strengths of width T/L_p around the critical value W_c.

In the presence of thermal fluctuations the free energy of adsorption f_W replaces the bare potential strength W and the free energy per length $g(f_d)$ of a thermally fluctuating, stretched semiflexible polymer replaces the force $-f_d$. For small stretching forces $f_d \ll T/L_p$, the polymer is effectively flexible and entropic elasticity gives $g(f_d) \approx -f_d^2 L_p/6T$, whereas for strong stretching $f_d \gg T/L_p$, we have $g(f_d) \approx -f_d + (2Tf_d/L_p)^{1/2}$, where the square root contribution is typical for semiflexible behavior [74, 41]. The polymer desorbs if the stretching free energy $g(f_d)$ compensates for the free energy cost of desorption, i.e., for $|g(f_d)| > |f_W|$. This gives a first order force-induced desorption transition (similar to DNA unzipping [75, 76], where the single strands are flexible polymers), at a critical force

$$f_{d,c} \approx \begin{cases} (6T|f_W|/L_p)^{1/2} & \text{for } |f_W| \ll 2T/L_p \\ |f_W| + (2T|f_W|/L_p)^{1/2} & \text{for } |f_W| \gg 2T/L_p \end{cases} \tag{59}$$

and, thus, the phase boundary of the adsorbed phase in the f_d-$|W|$ or f_d-T plane. The line of first order force-induced desorption transitions ends in the critical point of thermal desorption at zero force. The results for the phase diagram were confirmed by Monte Carlo (MC) simulations of a discretized semiflexible polymer, see Fig. 7a. The discretized semiflexible chain consists of $N = L_c/\Delta s$ beads with heights z_i (i.e., $h = z_N$) and $N-1$ connecting segments of length Δs with unit tangent vectors $\mathbf{t}_i$ using the Hamiltonian $\mathscr{H} = E_b + \sum_{i=1}^{N} \Delta s V(z_i) - f_d h$, where $E_b = (\kappa/2)\sum_{i=1}^{N-1}(\mathbf{t}_{i+1}-\mathbf{t}_i)^2/\Delta s$ is the bending energy. The analytical result (59) correctly describes three main features of the simulation results: (i) A characteristic square-root dependence $f_{d,c} \sim |f_{W,\mathrm{SF}}|^{1/2} \sim |T-T_c|^{1/2}$ close to the thermal desorption transition typical for flexible behavior. (ii) A broad *linear* regime $f_{d,c} \approx |f_W| \sim |T-T_c|$ at lower temperatures, which is absent for flexible polymers and due to the bending rigidity effects. (iii) At low temperatures $T < |W|\ell^{2/3}L_p^{1/3}$, we find $f_{d,c} \sim |W| - T^{4/3}/\ell^{2/3}\kappa^{1/3} + T|W|^{1/2}/\kappa^{1/2}$, which gives a small *reentrant* region of the desorbed phase because thermal fluctuations weaken the adhesion strength less than the pulling force. Such "cold desorption/unzipping" has been reported previously for flexible polymers like DNA [76].

The energy landscape of the desorption process can be mapped by calculating the *constrained* free energy $\Delta F(h) = -T\ln[Z(h)/Z(0)]$ where $Z(h)$ is the restricted partition sum over all polymer configurations with a given height h of the end point. The transfer matrix treatment of the weakly bent semiflexible polymer [69] gives the constrained free

energy

$$\Delta F(h) = -\frac{T}{2}\ln\left(\frac{h}{L_p}\right) + \frac{2^{7/4}}{3^{1/2}}h^{1/2}\kappa^{1/4}|f_W|^{3/4} \tag{60}$$

for the semiflexible regime $|f_W| \gtrsim T/L_p$. This is the exact generalization of the $T = 0$ result (56) for small h to finite temperatures, where the free energy of adsorption of a semiflexible polymer f_W replaces the bare contact potential W and a logarithmic entropic repulsion from the hard wall occurs. For large h, the free energy cost (60) is *always* exceeded by the linear energy gain $-f_d h$, which suggests the absence of a phase transition and a desorption instability even for small forces f_d [68].

However, the weak bending approximation breaks down upon increasing h if typical tangent angles $h/L_d > 1$ become large for $h > R_{co} \equiv (\kappa/2|f_W|)^{1/2}$. Then the whole desorbed tail of length L_d becomes lifted perpendicular to the substrate except for a curved segment of length $\sim R_{co}$, i.e., $L_d \approx h + \mathcal{O}(R_{co})$. In this limit the full free energy $\Delta G(h) = \Delta F(h) - hf_d$ in the presence of the desorbing force can be written as

$$\Delta G(h) \approx h[|f_W| + g(f_d)] + cR_{co}|f_W|, \tag{61}$$

where c is a numerical constant [$c = 4(\sqrt{2} - 1)$ at $T = 0$, see (56)]. Equation (61) is in accordance with our above free energy criterion $|g(f_d)| = |f_W|$ for the desorption transition.

Therefore, also for $T > 0$, the free energy landscape $\Delta G(h) = \Delta F(h) - hf_d$, as given by (60) for $h \lesssim R_{co}$ and (61) for $h \gg R_{co}$, exhibits a *barrier* for $f_d > f_{d,c}$, which arises from the bending rigidity although the microscopic adhesion potential is purely attractive. In the MC simulation, $\Delta G(h)$ can be calculated from the logarithm of the end point distribution function, which clearly confirms the existence of a barrier, see Fig. 7c. In the semiflexible regime for $|f_W| \gtrsim T/L_p$, we find an energy barrier $\Delta G_b \sim \kappa^{1/2}|f_W|^{3/2}/f_d$ for all forces $f_d > f_{d,c} \approx |f_W|$. The barrier scales with $\kappa^{1/2}$ and decreases as $1/f_d$ starting from $\Delta G_b \sim (\kappa|f_W|)^{1/2}$. The barrier is attained for a height $h \sim \Delta G_b/f_d$, which approaches $h \sim R_{co}$ for $f_d = |f_W|$. In the semiflexible regime $|f_W| \gtrsim T/L_p$, we have $\Delta G_b \gtrsim T$ and $R_{co} \lesssim L_p$. Upon entering the flexible regime the barrier becomes smaller than the thermal energy T and can thus be overcome quasi-spontaneously by thermal activation; the contact radius becomes larger than the Kuhn segment length L_p.

The existence of a barrier in the semiflexible regime has important consequences for single polymer desorption experiments. In equilibrium, the necessary desorption force $f_d(h) = \partial_h \Delta F(h) \propto h^{-1/2}$ *diverges* for small h, before a plateau of constant separation force $f_d = f_{d,c} \approx |f_W|$ is reached at large h. If the desorption experiment is performed out of equilibrium at constant desorption force larger than the threshold force, $f_d > f_{d,c}$, the energy barrier ΔG_b has to be overcome by thermal activation with an Arrhenius-type desorption rate which has a strong influence on the kinetics of *initial* desorption [52].

In summary, we presented the phase diagram for force-induced desorption of semiflexible polymers and derived the existence of a characteristic energy barrier which is a consequence of the bending rigidity and absent for flexible polymers. Both results are confirmed by Monte Carlo simulations. The energy barrier gives rise to activated desorption kinetics and leads to an enhanced dynamic stability of the bound state of stiff adhesive polymers or fibers under force. This effect plays a role for biological poly-

mers under force, e.g., in DNA, protein, or filament unzipping and desorption as well as for numerous materials science applications ranging from the delamination of thin sheets to the peeling of adhesive hairs. The results can also shed new light on the zipping or adsorption dynamics of semiflexible filaments, which plays an important role in cytoskeletal networks [77].

SEMIFLEXIBLE POLYMERS ON STRUCTURED SUBSTRATES

Many applications in (bio-)nanotechnology, such as the construction of electric devices or sensors containing nanotubes, require immobilization, controlled shape manipulation, and positioning of semiflexible polymers. Adsorption on substrates is the simplest technique to immobilize single polymers and a first step towards further manipulation and visualization of structure details using, e.g. modern scanning probe techniques [24, 25]. Such scanning force techniques can be used to apply localized point forces to a polymer adsorbed on a substrate and force a lateral movement [31, 5]. Polymers that are strongly adsorbed onto crystalline substrates such as graphite or mica experience a spatially modulated adsorption potential reflecting the underlying crystal lattice structure and giving rise to preferred orientations of the adsorbed polymer. For such systems, the dynamics of the adsorbed polymer is governed by thermal activation over the potential barriers of the surface potential.

The thermally activated motion over a translationally invariant potential barrier has been studied in Refs. [78, 79, 80] for homogeneous and point driving forces. At low forces the activated dynamics is governed by the nucleation of localized kink-like excitations as shown in Fig. 9. The activated dynamics of semiflexible polymers is different from that of flexible polymers as kink properties are not governed by entropic elasticity of the polymer chain but rather by the bending energy of the semiflexible polymer. In principle, this allows to extract material parameters such as the persistence length or the height of substrate energy barriers from kink properties. The barrier crossing of the polymer requires kink nucleation, diffusion and recombination and time scales for barrier crossing and the mean velocity of the semiflexible polymer can be linked to the dynamic properties of kink excitations.

In this review we want to focus on another important aspect of structured adsorbing surfaces, which is the control of the shape of an adsorbed semiflexible polymer. The controlled adsorption of single carbon nanotubes at predefined positions, e.g. at electrodes, has been achieved by using chemically structured substrates [81, 82, 83]. The substrate patterns used in these experiments are composed of domains of arbitrary shape, which are characterized by a greater binding affinity compared to the surrounding substrate. Theoretically, this effect can be described by a laterally modulated adhesion potential, where, the polymer gains a constant adsorption energy $W < 0$ per unit length.

We will explore the possibility to gain such shape control for semiflexible polymer rings using simple striped surface structures. Examples of circular semiflexible polymers are provided by carbon nanotubes [84, 85], DNA minicircles [86], filamentous actin [87], and amyloid fibrils [88]. The substrate patterns studied in the following correspond to a single chemically striped domain, see Fig. 10a, and to a single topographical surface channel, see Fig. 10b. It turns out, that a shallow topographical step of a certain width

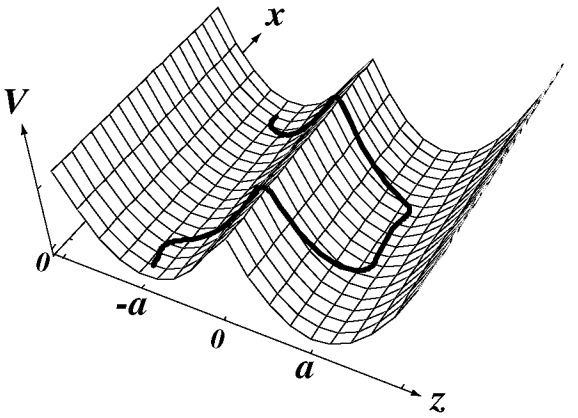

FIGURE 9. Typical conformation of a semiflexible polymer (thick line) with a kink-antikink pair in the xz-plane and in a translationally invariant double-well potential V, which depends on the coordinate z, is independent of the coordinate x, and has minima at $z = \pm a$.

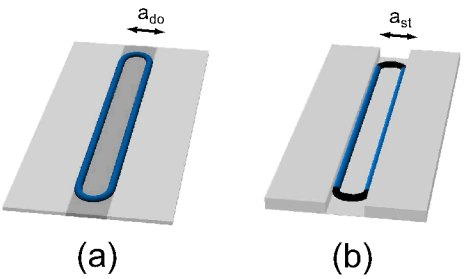

FIGURE 10. Adsorbed circular polymer on a striped surface containing (a) a chemically structured surface domain of width a_{do} and (b) two topographical surface steps forming a channel of width a_{st}.

has an effect very similar to a thin adhesive stripe, because the polymer is attracted to the surface steps. Such topographical surface steps have been employed in recent manipulation experiments on semiflexible polymer rings [89].

In the following, we will focus on the limit of persistence lengths much larger than the stripe width, where thermal fluctuations can be neglected. We find that the competition between the bending rigidity of the circular semiflexible polymer and its attraction to the striped domain allows a controlled switching between four distinct stable morphologies, see Fig. 11: Apart from a weakly bound almost circular shape (I) and a strongly bound confined shape (II_0), bulged intermediate shapes (II_1, II_2) become stable for large contour lengths. Our results are summarized in the full morphological diagrams for semiflexible ring shapes depending on the size of the ring compared to the size of the structure as well as the material parameters, namely, the bending rigidity κ and the adhesion energy gain W. This analysis can be used to (i) control the ring shape and (ii)

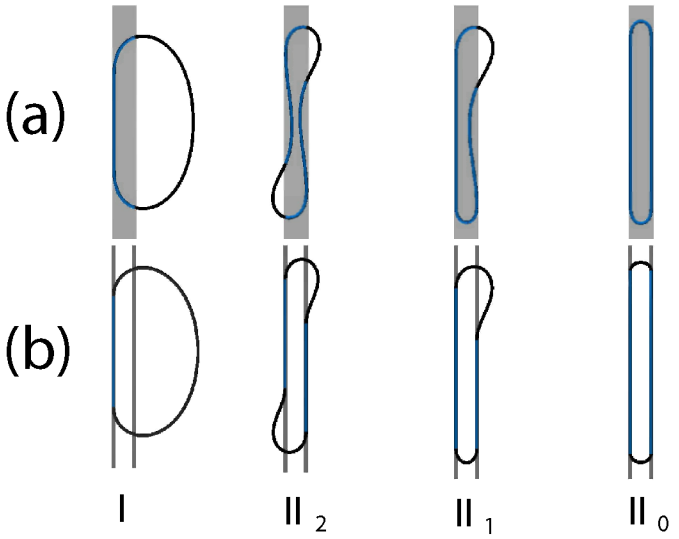

FIGURE 11. Top views of the four types of stable morphologies of a ring polymer adhering to a surface with a chemical domain (a) or topographical stripe (b) as obtained by energy minimization for contour lengths $L/a_{st} = 20$.

analyze material properties of the substrate or the semiflexible polymer ring experimentally. Flexible polymer rings, on the other hand, exhibit random coil configurations and such morphological transitions are absent.

We will first discuss topographical surface channels. We consider a planar substrate in the xy-plane that contains two parallel topographical surface steps at $x = \pm a_{st}/2$ forming an infinitely long surface channel of width a_{st}. A semiflexible polymer ring, characterized by the bending rigidity κ and the fixed contour length L, gains an overall adsorption energy $W_{st} < 0$ per polymer length by adsorbing to the substrate surface. At the edges of the surface channel the adsorption energy is doubled, since the semiflexible polymer can bind to two adjacent surfaces at the same time. We will refer to this extra energy contribution as the adsorption energy and omit the constant energy offset. The resulting effective lateral adsorption potential can be described by

$$V_{st}(x) = \begin{cases} W_{st} & \text{for } |x \pm a_{st}/2| < \ell/2, \\ 0 & \text{otherwise,} \end{cases} \tag{62}$$

where ℓ denotes the adhesive range of the steps, which is of the order of the polymer diameter and assumed to be small compared to the channel width, $\ell \ll a_{st}$. Furthermore, we neglect small energy corrections arising where the polymer crosses the surface steps, and kink configurations, similar to the one displayed in Fig. 9, will occur. The resulting confined shapes are therefore not a consequence of pure geometric constraints, but of the adsorption energy gain induced by the surface steps.

The bending energy of the polymer in the two-dimensional substrate plane is given by $E_b = (\kappa/2)\int_0^L ds(\partial_s\phi(s))^2$, where κ is the bending rigidity, and the contour is parameterized by the arc length s ($0 < s < L$) using the tangent angles $\phi(s)$, see (20). The adhered length L_{st} is given by the polymer length on the edges at $x = \pm a_{st}/2$, and the adhesion energy is $E_{ad} = -|W_{st}|L_{st}$. The polymer configuration is determined by minimizing the total energy $E_{\rm tot} = E_{ad} + E_b$ under the constraints imposed by ring closure, i.e., $\int_0^L ds(\cos\phi(s), \sin\phi(s)) = (0,0)$. This yields a shape equation for $\phi(s)$ and an implicit equation for the Lagrange multiplier. Solving these equations, the polymer shape and the resulting energies can be calculated analytically. Instead of an analytical solution to the variational problem we want to focus here on results from the numerical minimization of the total energy $E_{\rm tot} = E_{ad} + E_b$ using the dynamical discretization algorithm of the SURFACE EVOLVER 2.14 [90]. The contour of the polymer is discretized and represented by a set of vertices and directed edges, which connect neighboring vertices. The contour length of a shape segment is identified with the sum over the length of the corresponding edges and a discretized version of the bending energy is assigned to each vertex. The basic operations are the refinement of the discretization and energy minimization by a conjugate gradient algorithm. In order to determine all metastable states of the total energy $E_{tot} = E_b + E_{ad}$, we minimize the *constrained* energy, where we fix the adhered length L_{st} and, thus, the adhesion energy. In the presence of an additional constraint some metastable configurations can be stabilized.

Analyzing the total energy, one finds that two control parameters, which are combinations of the four parameters L, κ, a_{st} and W_{st}, are sufficient to characterize the system. In the following we measure lengths in units of the channel width and energies in units of the typical bending energy,

$$\bar{L} \equiv L/a_{st} \quad \text{and} \quad \bar{E} \equiv E a_{st}/\kappa, \tag{63}$$

which leads to a *reduced adhesion strength*

$$|w_{st}| \equiv |W_{st}|a_{st}^2/\kappa \quad \text{or} \quad |\tilde{w}_{st}| \equiv |W_{st}|L^2/\kappa = |w_{st}|\bar{L}^2. \tag{64}$$

The reduced parameters w_{st} and $\bar{L}$ are advantageous in discussing the control of shapes as a function of the contour length L, which changes the parameter $\bar{L}$ only. If the channel width a_{st} is varied, the reduced parameters $\tilde{w}_{st}$ and $\bar{L}$ are better suited because the channel width a_{st} then only changes the parameter $\bar{L}$ at constant $\tilde{w}_{st}$.

The numerical minimization gives the following results for the topographical channel. For small $|L_{st}|$, the ring will attach only to one step edge and adopt the rather round toroidal configuration I, see Fig. 10. For $L_{st} \gtrsim L/2$, conformations, where the ring binds to both step edges, will become relevant. These shapes may be classified by the number of bulges or segments outside the channel and are referred to as II_0, II_1, and II_2, accordingly, see Fig. 10. The energy landscape $\bar{E}_{\rm tot}(\bar{L}_{st})$ exhibits up to four local minima, representing the four different (meta-)stable ring morphologies I, II_0, II_1, and II_2. The round configuration I is the state of minimal energy for small $|w_{st}|$, whereas the adhesion energy gain dominates for large $|w_{st}|$, and the elongated shape II_0 becomes the only stable conformation. The morphological transition between these two shapes is *discontinuous* with a jump in the adhered length L_{st}. In the vicinity of this transition also

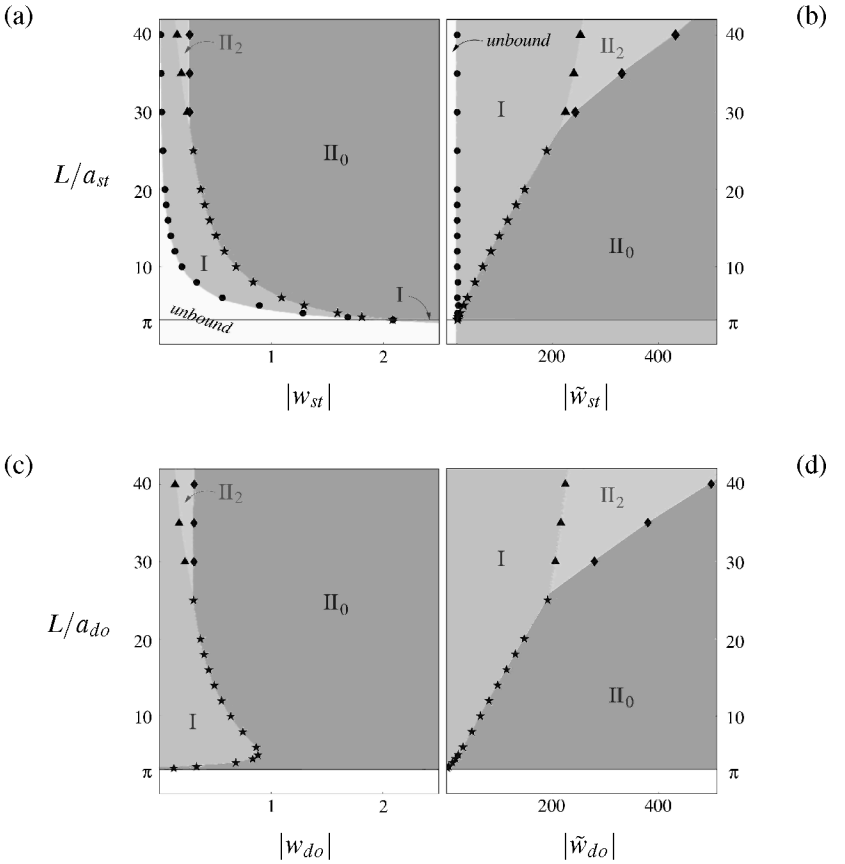

FIGURE 12. Morphology diagram for a ring polymer of length L adhering to the topographical surface channel of width a_{st} as a function of (a) L/a_{st} and $|w_{st}| \equiv |W_{st}|a_{st}^2/\kappa$ and (b) L/a_{st} and $|\tilde{w}_{st}| \equiv |W_{st}|L^2/\kappa$. If the topographical structure is replaced by a chemical domain of width a_{do} and adhesion strength $|W_{do}|$, the system is characterized by (c) L/a_{do} and $|w_{do}| \equiv |W_{do}|a_{do}^2/\kappa$ or (d) L/a_{do} and $|\tilde{w}_{do}| \equiv |W_{do}|L^2/\kappa$. The parameter choice in (b) and (d) is advantageous if the structure width a_{st} and a_{do} is varied, while the other system parameters are kept constant. Morphological transitions are obtained from numerical energy minimization and are represented by stars, triangles, diamonds and dots.

the shapes II$_1$ and II$_2$ can become stable or metastable, which develop from the elongated shape II$_0$ by the formation of one and two *bulges*, respectively. Shape I undergoes an additional unbinding transition from a single surface step, which is also known for vesicles adhering to a planar surface, where the interplay between adhesion and bending energy leads to an unbinding transition, which is not driven by thermal fluctuations [73].

These results can be summarized in morphology diagrams Figs. 12a and 12b. They show how the stability of the four shapes I, II$_0$, II$_1$ and II$_2$ and the unbound circle is controlled by the parameters $|w_{st}|$ and $\bar{L}$ (Fig. 12a) or $|\tilde{w}_{st}|$ and $\bar{L}$ (Fig. 12b). Morphology

boundaries from the numerical minimization procedure are denoted by stars, triangles, dots and diamonds. The main feature of the morphology diagram is the discontinuous transition between morphologies I and II_0 (stars). This transition line terminates at $\bar{L} = \pi$ and $|w_{st}| = 2$ where it intersects the unbinding transition line (dots) because a short ring can bind at most to one surface step. At the vertical transition line between configurations II_0 and II_2 (diamonds), which occurs for large $\bar{L}$, it becomes energetically favorable to form bulges on top of the confined shape II_0.

Now we turn to the chemically striped domain of width a_{do}, which is modeled by an additional adhesion energy gain $W_{do} < 0$ per polymer length for $|x| \leq a_{do}/2$, which leads to a generic square well adsorption potential with

$$V_{do}(x) = \begin{cases} W_{do} & \text{for } |x| \leq a_{do}/2, \\ 0 & \text{for } |x| > a_{do}/2. \end{cases} \tag{65}$$

The adhered length L_{do} is given by the polymer length within the stripe $|x| \leq a_{do}/2$, and the adhesion energy is $E_{ad} = -|W_{do}|L_{do}$.

Performing a numerical energy minimization we find the same four types of morphologies I, II_0, II_1, and II_2 as for the topographical surface channel, see Fig. 10(b). Remarkably, we find that ring shapes minimizing the bending energy are almost identical as compared to a topographical surface channel of the same width $a_{st} = a_{do}$, see Fig. 10. In contrast to the channel, the stripe domain is also adhesive between its boundaries for $|x| < a_{do}/2$ such that the same ring shape has a larger adhered length. This turns out to be the major difference between both types of stripes and leads only to approximately constant shifts in the adhered lengths.

Therefore the corresponding morphology diagrams Figs. 12c and 12d of the chemically structured surface domain look very similar to the morphology diagrams for the topographical stripes. In particular, the discontinuous transition between shapes I and II_0 (stars) and the appearance of stable bulged states along the vertical line between configurations II_0 and II_2 (diamonds) are very similar. However, the unbinding transition of shape I is absent for the chemical stripe domain: It is always energetically favorable for the ring to adhere to the striped domain. Furthermore, the two phase diagrams differ in the behavior of small rings. Small rings can fully bind to the chemical stripe without deformation and shapes I and II_0 become equivalent, which leads to the re-entrance of shape II_0 close to $L/a_{do} = \pi$.

In summary, the morphology diagrams in Figs. 12 give a complete classification of the morphologies of an adsorbed semiflexible polymer on a substrate containing an adhesive stripe domain, which can be either topographically or chemically structured. Applied to experiments such morphology diagrams allow a control of the shape of the adsorbed ring. Both types of structures lead to very similar behavior with a *discontinuous morphological transition* between the two dominant shapes I and II_0 and with intermediate bulged shapes II_1 and II_2 for large contour lengths.

CONCLUSION AND OUTLOOK

In this review we presented several examples of non-trivial equilibrium or zero temperature shapes of semiflexible polymers and on thermal fluctuations of these shapes. The examples – buckling, force-induced desorption, and shapes of adsorbed polymers on structured substrates – are motivated by single polymer manipulation experiments. At zero temperature the shapes can be calculated by minimizing the bending energy using variational methods, which leads to shapes composed of segments of different Euler Elastica. Thermal fluctuations are also governed by bending energy and display a distinct behavior different from flexible polymers.

In biological systems, filaments are not only subject to thermal forces. They are also constantly rearranged and reorganized by small forces generated by motor proteins or polymerization forces [12]. Both of these forces are generated by the hydrolysis of adenine triphosphate (ATP). This "active" filament dynamics gives rise to more complex non-equilibrium phenomena. One important example relevant to the buckling instability discussed in section is the buckling of a single polymerizing filament [23]. In systems containing many filaments and molecular motors active filament dynamics can lead to much more complex phenomena such as the formation of various filament patterns [91, 92, 93, 94, 95]. Issues related to filament pattern formation in *in vitro* systems, filament organization in the cytoskeleton, or force generation in the cell are subject of current research. Also in these active systems the shapes of filaments and their corresponding bending energies will play an important role.

ACKNOWLEDGMENTS

We acknowledge financial support by the Deutsche Forschungsgemeinschaft via Sonderforschungsbereich 448.

REFERENCES

1. P. G. De Gennes, *Scaling Concepts in Polymer Physics*, Cornell University Press, Ithaca, 1979.
2. M. Doi and S. F. Edwards, *The Theory of Polymer Dynamics*, Clarendon, Oxford, 1986.
3. A. Y. Grosberg and A. R. Khokhlov, *Statistical Physics of Macromolecules*, American Institute of Physics Press, New York, 1994.
4. E. M. Lifshitz and L. D. Landau, *Theory of Elasticity*, Pergamon Press, New York, 1986.
5. C. Ecker, N. Severin, L. Shu, A. D. Schlüter, and J. P. Rabe, *Macromolecules* **37**, 2484 (2004).
6. P. Samori, C. Ecker, I. Gössl, P. A. J. de Witte, J. J. L. M. Cornelissen, G. A. Metselaar, M. B. J. Otten, A. E. Rowan, R. J. M. Nolte, and J. P. Rabe, *Macromolecules* **35**, 5290.
7. D. G. Kurth, N. Severin, and J. P. Rabe, *Angew. Chem.* **114**, 3833 (2002).
8. C. Dekker, *Physics Today* **52**, 22, (1999).
9. W. H. Taylor and P. J. Hagerman, *J. Mol. Biol.* **212**, 363 (1990).
10. B. Alberts, D. Bray, J. Lewis, M. Raff, K. Roberts, J. D. Watson, *Molecular Biology of the Cell*, Garland Publishing, New York, 1994.
11. H. Lodish, A. Berk, L. S. Zipursky, P. Matsudaira, D. Baltimore, and J. Darnell, *Molecular Cell Biology*, W.H. Freeman, New York, 2000.
12. J. Howard, *Mechanics of Motor Proteins and the Cytoskeleton*, Sinauer Associates, Inc., Sunderland, 2001.
13. A. Ott, M. Magnasco, A. Simon, and A. Libchaber, *Phys. Rev. E* **48**, R1642 (1993).

14. F. Gittes, B. Mickey, J. Nettleton, and J. Howard, *J. Cell Biol.* **120**, 923 (1993).
15. J. Käs, H. Strey, and E. Sackmann, *Nature* **368**, 226 (1994).
16. J.-L. Barrat and J.-F. Joanny, *Advances in Chemical Physics, Vol. XCIV*, edited by I. Prigogine and S. A. Rice, John Wiley & Sons, New York, 1996.
17. O. Kratky and G. Porod, *Recl. Trav. Chim. Pays-Bas* **68**, 1106 (1949).
18. E. M. Lifshitz and L. D. Landau, *Statistical Physics, Part 1*, Pergamon Press, New York, 1969.
19. H. Kleinert, *Path Integrals in Quantum Mechanics, Statistics, and Polymer Physics, and Financial Markets*, World Scientific, Singapore, 2004.
20. G. Binnig, C. F. Quate, and C. Gerber, *Phys. Rev. Lett.* **56**, 930 (1986).
21. A. Ashkin, *Science* **210**, 1081 (1980).
22. S. B. Smith, L. Finzi, and C. Bustamante, *Science* **258**, 1122 (1992).
23. M. Dogterom and B. Yurke, *Science* **278**, 856 (1997).
24. S. S. Sheiko and M. Möller, *Chem. Rev.* **101**, 4099 (2001).
25. P. Samori, *J. Mater. Chem.* **14**, 1353 (2004).
26. M. Seitz, C. Friedsam, W. Jöstl, T. Hugel, and H. E. Gaub, *Chem. Phys. Chem.* **4**, 986 (2003).
27. B. Essevaz-Roulet, U. Bockelmann, and F. Heslot, *Proc. Natl. Acad. Sci. USA* **94**, 11935 (1997).
28. C. W. Jones, J. C. Wang, R. W. Briehl, and M. S. Turner, *Biophys. J.* **88**, 2433 (2005).
29. G. Binning and H. Rohrer, *Rev. Mod. Phys.* **59**, 615 (1987).
30. T. A. Jung, R. R. Schlittler, J. K. Gimzewski, H. Tang, C. Joachim, *Science* **271**, 181 (1996).
31. N. Severin, J. Barner, A. A. Kalachev and J. P. Rabe, *Nano Lett.* **4**, 577 (2004).
32. P. Gutjahr, R. Lipowksy, and J. Kierfeld, *Europhys. Lett.* **76**, 994 (2006).
33. P. G. De Gennes and C. Taupin, *J. Phys. Chem.* **86**, 2294 (1982).
34. R. Capovilla and J. Guven, *J. Phys. A: Math. Gen.* **38**, 2593 (2005).
35. W. Helfrich, *J. Physique* **46**, 1263 (1985); *ibid.* **47**, 321 (1986); *ibid.* **48**, 285 (1987).
36. L. Peliti and S. Leibler, *Phys. Rev. Lett.* **54**, 1690 (1985).
37. D. Förster, *Phys. Lett.* **114A**, 115 (1986).
38. H. Kleinert, *Phys. Lett.* **114A**, 263 (1986).
39. W. Helfrich, *Eur. Phys. J. B* **1**, 481 (1998).
40. H. Pinnow and W. Helfrich, *Eur. Phys J. E* **3**, 149 (2000).
41. J. Kierfeld, O. Niamploy, V. Sa-yakanit, and R. Lipowsky, *Eur. Phys. J. E* **14**, 17 (2004).
42. M. Abramowitz and A. I. Stegun, *Handbook of Mathematical Functions*, National Bureau of Standards, Washington, 1965.
43. T. Niemeijer and T. W. Ruijgrok, *Physica* **81A**, 427 (1975).
44. M. Nauenberg, *J. of Math. Phys.* **16**, 703 (1975).
45. F. Jülicher, R. Lipowsky, and H. Müller-Krumbhaar *Europhys. Lett.* **11**, 657 (1990).
46. H. Spohn, *Europhys. Lett.* **14**, 689 (1991).
47. K. Baczynski, R. Lipowsky, and J. Kierfeld, *Phys. Rev. E* **76**, 061914 (2007).
48. F. Gittes, E. Meyhöfer, S. Baek, and J. Howard, *Biophys. J.* **70**, 418 (1996).
49. M. Elbaum, D. Kuchnir Fygenson, and A. Libchaber, *Phys. Rev. Lett.* **76**, 4078 (1996).
50. J. Kierfeld, P. Gutjahr, T. Kühne, P. Kraikivski, and R. Lipowsky, *J. Comput. Theor. Nanosci.* **3**, 898 (2006).
51. L. R. G. Treloar, *The Physics of Rubber Elasticity*, Clarendon Press, Oxford, 1975.
52. J. Kierfeld, *Phys. Rev. Lett* **97**, 058302 (2006).
53. M. Rief, M. Gautel, F. Oesterhelt, J. M. Fernandez, H. E. Gaub, *Science* **276**, 1109 (1997).
54. S. B. Smith, L. Finzi, C. Bustamante, *Science* **258**, 1122 (1992).
55. S. Smith, Y. Cui, and C. Bustamante, *Science* **271**, 795 (1996).
56. T. J. Senden, J.-M. di Meglio, and P. Auroy, *Eur. Phys. J. B* **3**, 211 (1998).
57. X. Chatellier, T. J. Senden, J.-F. Joanny, and J.-M. Di Meglio, *Europhys. Lett.* **41**, 303 (1998).
58. T. Hugel, M. Grosholz, H. C. Clausen-Schaumann, A. Pfau, H. E. Gaub, and M. Seitz, *Macromolecules* **34**, 1039 (2001).
59. S. Cui, C. Liu, and X. Zhang, *Nano Lett.* **3**, 245 (2003).
60. C. Friedsam, A. Del Campo Becares, U. Jonas, M. Seitz, and H. E. Gaub, *New J. Phys.* **6**, 9 (2004).
61. T. M. Birshtein, E. B. Zhulina, and A. M. Skvortsov, *Biopolymers* **18**, 1171 (1979).
62. A. C. Maggs, D. A. Huse, and S. Leibler, *Europhys. Lett.* **8**, 615 (1989).
63. G. Gompper and T. Burkhardt, *Phys. Rev. A* **40**, 6124 (1989).
64. C. C. van der Linden, F. A. M. Leermakers, and G. J. Fleer, *Macromolecules* **29**, 1172 (1996).

65. R. R. Netz and J.-F. Joanny, *Macromolecules* **32**, 9013 (1999).
66. S. Stepanow, *J. Chem. Phys.* **115**, 1565 (2001).
67. A. N. Semenov, *Eur. Phys. J. E* **9**, 353 (2002).
68. P. Benetatos and E. Frey, *Phys. Rev. E* **67**, 051108 (2003).
69. J. Kierfeld and R. Lipowsky, *Europhys. Lett.* **62**, 285 (2003).
70. J. Kierfeld and R. Lipowsky, *J. Phys. A: Math. Gen.* **38**, L155 (2005).
71. E. Y. Kramarenko, R. G. Winkler, P. G. Khalatur, A. R. Khoklov, and P. Reineker, *J. Chem. Phys.* **104**, 4806 (1996).
72. T. Sintes, K. Sumithra, and E. Straube, *Macromolecules* **34**, 1352 (2001).
73. U. Seifert and R. Lipowsky, *Phys. Rev. A* **42**, 4768 (1990).
74. J. F. Marko and E. D. Siggia, *Macromolecules* **28**, (1995) 8759.
75. D. K. Lubensky and D. R. Nelson, *Phys. Rev. Lett.* **85**, 1572 (2000); *Phys. Rev. E* **65**, 031917 (2002).
76. D. Marenduzzo, A. Trovato, and A. Maritan, *Phys. Rev. E* **64**, 031901 (2001).
77. W. H. Roos, A. Roth, J. Konle, H. Presting, E. Sackmann, and J. P. Spatz, *Chem. Phys. Chem.* **4**, 872 (2003).
78. P. Kraikivski, R. Lipowsky, and J. Kierfeld, Europhys. Lett. **66**, 763 (2004).
79. P. Kraikivski, R. Lipowsky, and J. Kierfeld, Eur. Phys. J. E **16**, 319 (2005).
80. P. Kraikivski, R. Lipowsky, and J. Kierfeld, Europhys. Lett. **71**, 138 (2005).
81. M. Burghard, G. Duesberg, G. Philipp, J. Muster, and S. Roth, *Adv. Mater.* **10**, 584 (1998).
82. J. Liu, M. J. Casavant, M. Cox, D. A. Walters, P. Boul, W. Lu, A. J. Rimberg, K. A. Smith, D. T. Colbert, and R. E. Smalley, *Chem. Phys. Lett.* **303**, 125 (1999).
83. Y. Wang, D. Maspoch, S. Zou, G. C. Schatz, R. E. Smalley, and C. A. Mirkin, *Proc. Nat. Acad. Sci. USA* **103**, 2026 (2006).
84. R. Martel, H. R. Shea, and P. Avouris, *Nature* **398**, 299 (1999).
85. M. Sano, A. Kamino, J. Okamura, and S. Shinkai, *Science* **293**, 1299 (2001).
86. A. Amzallag, C. Vaillant, M. Jacob1, M. Unser, J. Bednar, J. D. Kahn, J. Dubochet, A. Stasiak, and J. H. Maddocks, *Nucl. Acid Res.* **34**, e125 (2006).
87. J. X. Tang, J. A. Käs, J. V. Shah, and P. A. Janmey, *Eur. Biophys. J.* **30**, 477 (2001).
88. D. M. Hatters, C. A. MacRaild, R. Daniels, W. S. Gosal, N. H. Thomson, J. A. Jones, J. J. Davis, C. E. MacPhee, C. M. Dobson, and G. J. Howlett *Biophys. J.* **85**, 3979 (2003).
89. N. Severin, W. Zhuang, C. Ecker, A. A. Kalachev, I. M. Sokolov, and J. P. Rabe, *Nano Lett.* **6**, 2561 (2006).
90. K. A. Brakke, *Exp. Math.* **1**, 141 (1992).
91. T. B. Liverpool and M. C. Marchetti, *Phys. Rev. Lett.* **90**, 138102 (2003).
92. K. Kruse, J. F. Joanny, F. Jülicher, J. Prost, and K. Sekimoto, *Phys. Rev. Lett.* **92**, 078101 (2004).
93. I. S. Aranson and L. S. Tsimring, *Phys. Rev. E* **71**, 050901(R) (2005).
94. F. Ziebert and W. Zimmermann, *Phys. Rev. E* **70**, 022902 (2004).
95. P. Kraikivski, R. Lipowsky, and J. Kierfeld, *Phys. Rev. Lett.* **96**, 258103 (2006).